

Genome-wide mapping of oncogenic pathways and genetic modifiers of chemotherapy using a high-risk hepatoblastoma genetic model

Jie Fang

St. Jude Children's Research Hospital

Shivendra Singh

St. Jude Children's Research Hospital

Sivaraman Natarajan

St. Jude Children's Research Hospital <https://orcid.org/0000-0003-2608-2887>

Heather Tillman

St. Jude Children's Research Hospital <https://orcid.org/0000-0002-9623-2812>

Ahmed Abuzaid

St. Jude Children's Research Hospital

Adam Durbin

St. Jude Children's Research Institute

HaWon Lee

St. Jude Children's Research Hospital

Qiong Wu

St. Jude Children's Research Hospital

Jacob Steele

St. Jude Children's Research Hospital

Jon Connelly

St. Jude Children's Research Hospital <https://orcid.org/0000-0002-5564-1775>

Changde Cheng

St. Jude Children's Research Hospital

Hongjian Jin

St. Jude Children's Research Hospital

Wenan Chen

St. Jude Children's Research Hospital <https://orcid.org/0000-0003-0379-2368>

Yiping Fan

Department of Computational Biology, St. Jude Children's Research Hospital

Shondra Pruett-Miller

St. Jude Children's Research Hospital <https://orcid.org/0000-0002-3793-585X>

Jerold Rehg

ST. JUDE CHILDREN'S RESEARCH HOSPITAL

Joseph Emmons

St. Jude Children's Research Hospital

Stefano Cairo

XenTech <https://orcid.org/0000-0002-4725-5970>

Ruoning Wang

The Ohio State University, The Research Institute at Nationwide Children's Hospital

<https://orcid.org/0000-0001-9798-8032>

Evan Glazer

University of Tennessee Health Science Center

Andrew Murphy

St. Jude Children's Research Hospital <https://orcid.org/0000-0001-6747-0355>

Taosheng Chen

St. Jude Children's Research Hospital <https://orcid.org/0000-0001-6420-3809>

Andrew Davidoff

The University of Tennessee Health Science Center <https://orcid.org/0000-0001-7900-2794>

John Easton

St Jude Children's Research Hospital <https://orcid.org/0000-0003-4503-6608>

Xiang Chen

St. Jude Children's Research Hospital <https://orcid.org/0000-0002-2499-8261>

Jun Yang (✉ jun.yang2@stjude.org)

St. Jude Children's Research Hospital <https://orcid.org/0000-0002-0770-9659>

Article

Keywords:

Posted Date: March 30th, 2022

DOI: <https://doi.org/10.21203/rs.3.rs-1438842/v1>

License:  This work is licensed under a Creative Commons Attribution 4.0 International License.

[Read Full License](#)

Version of Record: A version of this preprint was published at Nature Communications on July 6th, 2023. See the published version at <https://doi.org/10.1038/s41467-023-39717-6>.

Abstract

A lack of relevant genetic models and cell lines hampers our understanding of hepatoblastoma pathogenesis and the development of new therapies for this neoplasm. We report a liver-specific MYC-driven hepatoblastoma murine model that faithfully recapitulates the pathological features of mixed fetal and embryonal hepatoblastoma, with transcriptomics resembling the high-risk gene signatures of the human disease. Single-cell RNA-sequencing and spatial transcriptomics identified distinct subpopulations of hepatoblastoma cells. After deriving cell lines from the mouse model, we mapped the cancer dependency genes using CRISPR-Cas9 screening and identified druggable targets shared with human hepatoblastoma (i.e., CDK7, CDK9, PRMT1, PRMT5). Our screen also revealed oncogenes and tumor suppressor genes in hepatoblastoma that engage multiple, druggable cancer signaling pathways. Chemotherapy is critical for human hepatoblastoma treatment. A genetic mapping of doxorubicin response by CRISPR-Cas9 screening identified modifiers whose loss-of-function synergizes with (e.g., PRKDC) or antagonizes (e.g., apoptosis genes) with the effect of chemotherapy. The combination of PRKDC inhibition and doxorubicin-based chemotherapy greatly enhances therapeutic efficacy. These studies have provided a useful set of resources including disease models suitable to identify and validate potential therapeutic targets in human high-risk hepatoblastoma.

Introduction

Hepatoblastoma and hepatocellular carcinoma (HCC) are the most common primary liver malignancies in children and adolescents/young adults. While primary liver cancers account for only 1–2% of all pediatric tumors¹, the largest incidence increase has been observed for hepatoblastoma in children under 5 years in nearly all regions of the world². The rate is increasing at more than 4.3% annually in the US³. Hepatoblastoma is an embryonal neoplasm that likely arises from hepatic cell precursors^{4,5}. Genetically, hepatoblastoma has the fewest somatic mutations among all human cancers⁶, suggesting that hepatic precursor cells during the early stage of liver development may be particularly susceptible to events resulting in oncogenic transformation. In line with previous findings as reviewed^{7,8}, genomic sequencing studies have confirmed that mutations in the Wnt-β-catenin signaling pathway are the most common genetic event in hepatoblastoma^{9–17}. The gene for the antioxidant transcription factor, *NFE2L2*, is also altered in a subpopulation of high-risk hepatoblastomas^{9,10,15,17}, suggesting that liver cells undergo oxidative stress during cellular transformation or disease progression.

The Hippo signaling pathway plays a critical role in liver organogenesis and cancer^{18–20}. The dysregulated downstream effector molecule of Hippo signaling, YAP1, is involved in hepatoblastoma tumorigenesis^{21–25}. Hepatic developmental pathways may determine the differentiation capacity of mutated liver progenitor/stem cells, and differentiation status may determine the aggressiveness of hepatoblastoma⁹. Hepatoblastomas with high expression levels of stem cell markers (*EpCAM*, *LIN28B*, *SALL4*, *HMGA2*, *AFP*) are usually associated with poor prognosis⁹. Such “liver progenitor” cells could

accumulate massive loads of chemotherapy-induced mutations, leading to development of heavily mutated tumors with propensity for relapse and metastasis¹⁷.

The *MYC* oncogenes are involved in many cancers including hepatoblastoma^{11,26-30}. Gain of chromosome 2 and 8 (with *MYCN* and *MYC* oncogenes, respectively) is common (25%-50%) in hepatoblastoma^{7,11,31,32}. While β -catenin mutation alone (*CTNNB1*) is unable to transform hepatoblastoma, *MYC* can cooperate with β -catenin to drive tumorigenesis²⁸ and is required for tumor maintenance in a β -catenin-based hepatoblastoma mouse model²⁷. β -catenin drives *MYC* expression²⁹ and *MYC* silencing prevents tumor growth in human hepatoblastoma cancer cell line-based xenograft models¹¹. These data indicate that *MYC* plays an essential role in hepatoblastoma.

Due to a lack of targetable somatic mutations and paucity of genetic animal disease models and cell lines^{33,34}, identification of therapeutic targets in hepatoblastoma remains challenging. Conventional chemotherapy is critical for most hepatoblastoma treatment. However, the genetic response of hepatoblastoma cells to chemotherapy is not well defined, which impedes development of more effective therapies because of an incomplete understanding of the mechanism of therapeutic response and resistance. Here we generated a hepatocyte-specific *MYC*-driven multifocal hepatoblastoma model that resembles high-risk human hepatoblastoma. We characterized the transcriptomics (both bulk RNA-seq and scRNA-seq) and spatial transcriptomics of this transgenic hepatoblastoma model. We also created cell lines from this model that were readily passaged *in vitro* and mapped the cancer dependency genes using a genome-wide CRISPR-Cas9 screening approach. We also performed genetic mapping of cellular responses to doxorubicin, a commonly used chemotherapeutic for hepatoblastoma treatment, with a genome-wide CRISPR-Cas9 screen and identified genes that synergized with and antagonized the effect of chemotherapy. Based upon this screen, we developed a combination therapy that showed better efficacy than doxorubicin treatment alone. Our studies have characterized useful disease models (mouse and cell lines) and identified potential therapeutic targets of hepatoblastoma that are conserved across species.

Results

Hepatocyte-specific *MYC* overexpression drives rapid hepatic oncogenesis

Previous genetic hepatoblastoma mouse models have provided invaluable information toward our understanding the role of oncogenic drivers. However, these models have only addressed well differentiated hepatoblastoma, which has a good outcome, or they do not align with the onset of liver development in children. To overcome these caveats, we generated a new model by crossing hepatocyte-specific transgenic Alb-Cre mice (Cre recombinase under the control of the mouse albumin enhancer/promoter hybrid)³⁵ with CAG-STOP^{flox/flox}-Myc mice (CAG promoter-driven human c-MYC, whose expression is prevented by a loxP site flanked STOP cassette)³⁶ (**Figure 1A**). Hepatocyte-specific Cre-mediated excision of the floxed STOP cassette allows expression of the CAG promoter-driven

human *Myc*, leading to a typical phenotype with hepatomegaly and paraneoplastic alopecia in double transgenic *Alb-Cre;CAG-Myc* mice (ABC-Myc, **Figures 1B and S1A**). Strikingly, activation of one allele of the *Myc* oncogene led to rapid onset of liver tumors and all of these mice died within 1-10 weeks after birth (**Figure 1C**). However, embryonic lethality was not induced by *Myc* activation as all possible genotypes were recovered at the expected Mendelian ratio (**Table S1**). Western blot and immunohistochemistry validated MYC overexpression in livers and tumor tissues at fetal (E17.5) and different postnatal stages (**Figures 1D, S1B**), suggesting that MYC is activated in the fetal stage. In parallel, we also developed an ABC-Myc;TdTomato model, which had a similar tumor penetrance and expressed TdTomato as a lineage reporter (**Figure 1C**). These data demonstrate that MYC alone is sufficient to quickly drive tumorigenesis in this transgenic model that aligns with the onset of liver development in children.

Pathological analyses define the ABC-Myc-driven liver neoplasm as hepatoblastoma

Hepatoblastoma is histologically heterogenous, with three main histologic patterns (epithelial, mixed epithelial, and mesenchymal). Epithelial patterns are further delineated into fetal, embryonal, mixed fetal and embryonal, cholangiocytic, small cell undifferentiated, macrotrabecular, and others^{37,38}. Hepatoblastomas arising in the ABC-Myc-driven cancer model effaced most of the sampled liver tissues and had combinations of both fetal and embryonal morphologies comprising the bulky tumors as well as scattered foci of extramedullary hematopoiesis (**Figures 1E and S1C**), the most common histologic type observed in human hepatoblastoma. The neoplastic subpopulations that maintained a fetal morphology had cytological atypia, with enlarged nuclei and prominent nucleoli, as well as variable cytoplasmic vacuolation of neoplastic hepatocytes caused by the accumulation of intracellular glycogen and/or lipid. The cancer cells with an embryonal morphology were arranged in nests and glandular and acinar structures with occasional pseudorosettes observed. Neoplastic cells with an embryonal morphology also had amphophilic to basophilic, granular cytoplasms, lacked cytoplasmic vacuolation, had angular nuclei, maintained higher nuclear:cytoplasmic ratios, and had increased mitotic activity. We further determined the pathological features of the liver neoplasms using immunohistochemistry (**Figures 1F-J and S1D-H**), for examination of alpha fetoprotein (AFP, **Figures 1F and S1D**), a stem cell marker indicating neoplastic hepatocellular cells³⁸, arginase-1 (ARG-1, **Figures 1G and S1E**), a marker to distinguish primary hepatocellular tumor from a non-hepatocellular metastasis to the liver³⁹, and glutamine synthetase (GS, **Figures 1H and S1F**), a b-catenin target and an indicator of hepatoblastoma^{37,38}. Both AFP and GS markers had diffuse immunoreactivity that was localized to the cytoplasm of neoplastic cells in all sampled tumors, and ARG1 was also diffusely immunopositive. Neoplastic populations were determined to be immunonegative for cytokeratin 19 (KRT19, **Figures 1I and S1G**), a marker used to identify cholangiocytic elements³⁷, although non-neoplastic, entrapped bile ducts had immunoreactivity. As b-catenin is a critical driver of hepatoblastoma, we also examined the expression of total form of this marker, which showed immunoreactivity that was localized to both the membrane and

cytoplasm of neoplastic populations with both fetal and embryonal morphologies (**Figures 1J and S1H**), suggesting that the Wnt pathway is selectively activated during tumorigenesis. Nevertheless, the lack of strong nuclear translocation of the wild-type b-catenin may suggest that MYC overactivation relieves the selective pressure on b-catenin, since MYC is a key downstream effector of the Wnt-b-catenin pathway^{26,29,40}. Nevertheless, human embryonal hepatoblastoma may not always have b-catenin expression that is localized to the nucleus³⁷. In summary, the ABC-Myc hepatoblastoma model recapitulates morphologic and immunohistochemical features of both fetal and embryonal morphologies that are observed in human hepatoblastomas.

Serum chemistry panel analysis reveals liver dysfunction of ABC-Myc mice

To assess the liver functions of ABC-Myc mice, we performed serum chemical analysis (**Table 1**). Not surprisingly, ABC-Myc mice showed abnormal elevation of alkaline phosphatase (ALP), alanine transaminase (ALT), and total bilirubin, the three commonly used biomarkers of liver function, indicating that the livers in ABC-Myc mice are damaged. One clinical study showed that 80% of hepatoblastoma patients had abnormal levels of ALP and 12.5% had increased ALT⁴¹. As liver is the major organ that produces glucose, liver cancer can cause hypoglycemia. Indeed, the serum glucose levels in ABC-Myc mice were remarkably reduced. The serum levels of creatinine and blood urea nitrogen (BUN) in ABC-Myc mice were also declined in comparison with the age-matched normal mice. While creatinine and BUN are the commonly used chemical markers to assess kidney function, liver cancer can lead to less production of creatinine, a break-down product of creatine in liver through transamination of amino acids. Low levels of BUN may indicate liver disease in the clinic which leads to less production of urea. However, the albumin and globulin levels seemed to be in the normal range, and no abnormal levels of common electrolytes (Sodium, Potassium, Calcium and Phosphorous) were observed (**Table 1**). We further performed complete blood count (CBC) measurements to assess if ABC-Myc mice had developed additional complications. While white blood cell counts showed no difference between normal mice and ABC-Myc mice, the absolute number and percentage of circulating eosinophils tended to be increased although they were not statistically significant (**Table 2**). However, the ABC-Myc mice developed microcytic anemia, as indicated by reduction of proportion of red blood cells (hematocrit, HCT%), amount of hemoglobin (HB), mean corpuscular volume (MCV) and mean corpuscular hemoglobin (MCH), increase in size variation (percentage of red cell distribution width, RDW%), but normal range of total number of red blood cells and mean corpuscular hemoglobin concentration (MCHC). Thrombocytosis also occurred in ABC-Myc mice, as indicated by an increase in total platelet counts, plateletcrit (PCT), and mean platelet volume (MPV) (**Table 2**). One study reported that among hepatoblastoma patients, 75% had thrombocytosis and 37.5% had microcytic anemia, whereas only 23.1% of pediatric HCC patients had thrombocytosis and none had microcytic anemia⁴². These chemistry and CBC parameters are consistent with the presence of hepatoblastoma in ABC-Myc mice.

Signaling pathways in ABC-Myc tumor cells resemble those in human hepatoblastoma with a poor outcome

To understand the molecular mechanisms of ABC-Myc hepatoblastoma, we identified the differentially expressed genes in tumors versus age-matched normal murine livers using bulk RNA-seq (**Figure 2A** and **Table S2**), followed by signaling pathway analysis. Interestingly, the *Igf2* oncogene ranked first (log₂ fold change = 11.6) among the upregulated genes in tumors (**Figure 2A**). In human, *IGF2* is located in the 11p15.5 imprinted locus, which is the second most frequently altered locus in hepatoblastomas and hepatocellular carcinomas, mostly through copy-neutral loss of heterozygosity¹⁷. *IGF2* induction by 11p15.5 alterations is likely the first genetic event in hepatoblastoma¹⁷. However, the most significantly downregulated genes in tumors were cytochrome P450 (CYP) family genes related to metabolic functions of mature hepatocytes (**Figure 2A**). Gene set enrichment analysis (GSEA)⁴³ showed that the genes upregulated in ABC-Myc tumors were significantly associated with gene signatures upregulated in liver cancers⁴⁴ (**Figure 2B**), and specifically upregulated by MYC in liver cancer⁴⁵ (**Figure 2C**). Conversely, the downregulated genes in the ABC-Myc tumor cells were significantly associated downregulated gene sets in human hepatoblastoma¹¹ (**Figure S2A**), downregulated by MYC in liver cancers⁴⁵ (**Figure S2B**), and associated with downregulation of HNF1A targets⁴⁶ (**Figure S2C**). Importantly, the b-catenin pathway was significantly upregulated in ABC-Myc tumors (**Figure 2D**). To determine if ABC-Myc induces transcriptomes similar to those in human hepatoblastoma, we cross-referenced our RNA-seq results for the top 500 genes upregulated and downregulated in ABC-Myc tumors with human RNA-seq analysis⁴⁷ or microarray studies⁹. The results revealed that the top differentially expressed genes in ABC-Myc tumors were also similarly altered in human hepatoblastomas (**Figures 2E and S2D**), suggesting that the murine hepatoblastoma model resembles human disease at the transcriptomic levels. Further comparison of the gene pathways between ABC-Myc tumors and human hepatoblastomas revealed that both shared altered metabolic pathways and those regulating the cell cycle, DNA replication and repair, and RNA splicing (**Table S3**).

Consistent with the embryonal histological features, GSEA results showed that ABC-Myc tumors had significant upregulation of cancer stem cell signatures including “liver cancer with upregulated EpCAM” (**Figure 2F**), and “undifferentiated cancer” (**Figure 2G**). Compared with the age-matched normal livers, the hepatoblastoma embryonic gene markers (i.e., *Lin28b*, *Sall4*, *EpCAM*, *Hmga*, *Afp*) in ABC-Myc tumors, which are usually associated with a poor outcome⁹, were increased over 4~250 fold (**Figure 2A, Table S2**). Notably, *Lin28b* is an oncogene that can drive hepatoblastoma in a transgenic mouse model⁴⁸, and is highly expressed in high-risk hepatoblastoma³⁰. *DLK1* is a well-known hepatoblast marker and is highly expressed in hepatoblastoma⁴⁹. Carrillo-Reixach et al recently identified the *DLK1-DIO3* locus genes on 14q32 as a new hallmark of human hepatoblastoma that is associated with Wnt/b-catenin signaling, and high expression of 14q32 gene signature is associated with a poor outcome¹⁵. In line with these findings in human hepatoblastoma, *Dlk1* was highly expressed in ABC-Myc tumors (log₂ fold

change = 8.85) (**Table S2**), suggesting that hepatoblast could be the cell of origin of ABC-Myc hepatoblastoma. The outcomes of hepatoblastoma can be distinguished by two molecular signatures, C1 and C2, which represent better and worse outcomes, respectively¹¹. We cross-referenced C1 and C2 signatures to our RNA-seq data and found that ABC-Myc tumors expressed higher levels of C2 and lower levels of C1 signatures (**Figure 2H**). To further validate ABC-Myc tumors represent C2 class, we applied seven different prediction algorithms¹¹, and all of which showed that ABC-Myc hepatoblastomas were classified as C2 (**Table S4**). Hirsch et al reported that hepatoblastoma can be further classified into 4 molecular subtypes, ‘Hepatic differentiation’, ‘Liver progenitor’, ‘Mesenchymal’ and ‘Proliferation’¹⁷. ABC-Myc tumors exhibited low expression of ‘Hepatic differentiation’ signature, but high expression of the ‘Liver progenitor’ and ‘Proliferation’ signatures (**Figure 2I**). We also found three out of six ‘Mesenchymal’ markers were expressed in ABC-Myc tumors (**Figure 2I**), albeit to a lesser degree (**Table S2**). While the ‘Hepatic differentiation’ group overlaps with C1, the ‘Liver progenitor’ signature is associated with a subclass of hepatoblastoma that has the worst outcome^{15,17}. Taken together, these data indicate that ABC-Myc tumors resemble human hepatoblastoma with molecular signatures of poor outcome.

ABC-Myc tumors and human hepatoblastoma exhibit dysregulated NAD⁺ metabolic pathways

Mature hepatocytes are responsible for the coordinated regulation of essential human metabolic processes. Differentiation blockade in hepatoblastoma is therefore expected to be associated with dysregulation of normal metabolic processes. The downregulation of comparable metabolic pathways in KEGG (i.e., xenobiotics metabolism by cytochrome P450, pyruvate metabolism, steroid hormone biosynthesis) in both ABC-Myc tumors and human hepatoblastomas further demonstrates that this genetic model resembles human liver cancers (**Table S3**) and supports a model of MYC-mediated hepatoblast differentiation arrest. In particular, tryptophan catabolism is one of the most significantly altered metabolic pathways in hepatoblastoma across species (**Figures 3A, 3B and S3A, 3B**). Tryptophan is an essential amino acid but only a small fraction of free tryptophan is used for protein synthesis and the production of neurotransmitters⁵⁰. Over 95% of free tryptophan is degraded by TDO2 (Tryptophan 2,3-Dioxygenase) and IDO (Indoleamine 2,3-Dioxygenase), resulting in production of kynureneine⁵¹, an important immunomodulatory factor. Kynureneine is further metabolized by a series of enzymes including KMO (Kynureneine 3-Monoxygenase) and KYNU (Kynureninase), and finally catabolized to oxidized nicotinamide adenine dinucleotide (NAD⁺)⁵¹. This process is the sole route for de novo synthesis of NAD⁺ (**Figure 3C**). The NAD⁺ salvage pathway involves enzymes such as NMNAT (nicotinamide mononucleotide adenylyl transferase) that synthesizes NAD⁺ from nicotinamide mononucleotide (NMN) (**Figure 3C**). NAD⁺ and its reduced nicotinamide adenine dinucleotide (NADH) play important roles in diverse biological processes, from oxidative phosphorylation and redox reactions to regulation of gene transcription and DNA repair⁵¹. Our RNA-seq analysis showed that all the genes encoding key enzymes in de novo and salvage synthesis of NAD⁺ were significantly downregulated in ABC-Myc liver tumors (**Table S2, Figure 3C**). Western blot validated that the expression of TDO2 and IDO2 was remarkably

reduced in ABC-Myc liver tumors (**Figure 3D**). We further assessed the levels of NAD⁺ and NADH in liver tumors in comparison with the age-matched normal livers. The results showed that NAD⁺ and NADH in ABC-Myc hepatoblastoma were significantly reduced (**Figure 3E**). Interestingly, one study showed that restoration of NAD⁺ by providing mice a nicotinamide riboside diet can prevent tumor formation in a hepatocellular carcinoma model driven by unconventional prefoldin RPB5 interactor (URI)⁵², which suggests that NAD⁺ plays a role in liver cancer progression. We hypothesized that the dysregulation of metabolic pathways such as reduced production of NADH and NAD⁺ might induce oxidative stress, consequently leading to activation of the antioxidant pathways. Indeed, the NFE2L2 target genes were greatly upregulated in liver cancer compared with mouse normal livers (**Figure 3F**). NFE2L2 is a master transcriptional factor regulating expression of antioxidant genes (*Nqo1* and those involved in glutathione metabolism) and found to be mutated in a subclass of hepatoblastoma with a poor outcome. Taken together, these data indicate that the ABC-Myc liver tumors share dysregulated metabolic pathways with human hepatoblastoma.

scRNA-seq and spatial transcriptomic analysis of ABC-Myc tumors reveals the heterogeneity of hepatoblastoma cells

Single cell RNA sequencing (scRNA-seq) studies have shown that mammalian liver is composed of multiple cell lineages in addition to hepatocytes and cholangiocytes⁵³⁻⁵⁵. The heterogeneity of liver cells is further complicated by the anatomical structure of liver zonation^{56,57}, which shows a distinct expression pattern of metabolic genes from central vein to portal vein along the lobule axis⁵⁸. While scRNA-seq analysis has provided insight into adult hepatocellular carcinoma and its tumor microenvironment^{59,60}, tumor heterogeneity and stroma-tumor interaction in hepatoblastoma remain largely unknown. To capture the transcriptomic ecosystem of the ABC-Myc-driven tumors, we performed single-cell RNA-sequencing (scRNA-seq) to define the distinct cellular populations of 11,696 cells dissected from a tumor mass. On average, 43,725 reads were obtained per cell and the median gene number captured in each cell was 940. Cluster membership analysis identified 14 subgroups of cells (**Figures 4A**), which consisted of different stromal cells including myeloid cells (*Cd14⁺*), macrophages (*Cd68⁺*), T cells (*Cd3D⁺*, *Cd8A⁺*) and B cells (*CD19⁺*), endothelial cells (*Kdr⁺*) and cells expressing neuronal lineage markers (*Chgb⁺*) (**Figure S4A**). Interestingly, we identified a large group of cells expressing adult hemoglobin gene markers such as *Hba-a1* (**Figure 4B**), which was distinct from the subgroup expressing high level of *Afp*. To further characterize the origins of these distinct subpopulations of cells, we analyzed spatial transcriptomics of tumor tissues (**Figure 4C**), in which neoplastic and normal cells were pathologically defined under microscope. While *Afp* unequivocally labeled the areas with neoplastic cells, the *Hba-a1* high population cells were also found in cancer cells. Moreover, the expression patterns of *Afp* and *Hba-a1* were largely distinct (**Figure 4D**). These data indicate that ABC-Myc cancer cells are heterogenous and include one subpopulation with high levels of hemoglobin genes. To determine whether this is species-specific, we analyzed RNA-seq data of human hepatoblastoma cohort⁴⁷, and

indeed found that several hemoglobin genes were also highly expressed in a subpopulation of human hepatoblastoma (**Figure 4E**). A recent study also found that a subgroup of high-risk embryonal hepatoblastomas express high levels of hemoglobin genes¹⁴. Although not statistically significant, the expression between *AFP* and *HBD* (one of the adult human globin genes) tended to be negatively correlated in human hepatoblastoma tumors (**Figure 4F**), similar to the spatial expression pattern of *Afp* and *Hba-a1* in ABC-Myc tumors.

We further examined the spatial expression of hepatocyte genes. In line with our bulk RNA-seq data, the liver-specific genes including *Alb*, *Tdo2*, *Cyp2e1* and *Hpx* were all downregulated in neoplastic cells in comparison with the neighboring normal liver cells (**Figure 4G**). While T cells (*Cd3g*) and B cells (*Cd19*) were sparsely distributed across the tumor tissues (**Figure S4B**), the ABC-Myc tumor mass was enriched with macrophages (*Cd68*), stellate cells (*Cola1*) and endothelial cells (*Kdr*) (**Figure S4B**). Immunohistochemical staining further validated that T cells in ABC-Myc tumors were sparse, however, tumor associated macrophages were abundant, suggesting that the ABC-Myc environment is immunosuppressive (**Figure S4C**). This is consistent with the observations that tumors in children often show limited immune cell infiltration and thus considered immunologically “cold” tumors⁶¹.

Genome-wide screen of cancer dependency genes in an ABC-Myc-derived hepatoblastoma cell line

As a rare cancer and because of lack of relevant disease models, drug-actionable targets in hepatoblastoma have only rarely been reported. To identify the dependency genes of hepatoblastoma, we established cell lines from ABC-Myc tumors, which can be readily passaged *in vitro* in standard DMEM media. We used one of these highly aggressive cell lines, NEJF10, to conduct a genome-wide, pooled CRISPR-Cas9 screening to uncover new therapeutic targets of hepatoblastoma (**Figure 5A**). We identified 894 essential genes that are required for NEJF10 survival ($p<0.001$, FDR<0.05) (**Figure 5B, Table S5**), including 100 targets with inhibitors available (**Table S6**), and 27 tumor suppressive genes ($p<0.001$, FDR<0.2) whose knockouts lead to increased proliferation (**Figure 5C, Table S5**). Pathway enrichment analysis of the 894 essential genes using the ‘Genetic and Chemical Perturbation database’ showed that they are enriched in class 2 hepatoblastoma genes, and are targets of BMP2, DREAM complex, MYC and b-catenin (**Figure 5D**). Biocarta and KEGG pathway analyses showed that these essential genes are involved in a variety of biological functions (spliceosome, proteasome, DNA replication and repair, translation, metabolism, etc.) (**Figures S5A, S5B**). Network analysis revealed that many of these essential genes formed a functional network (**Figures S5C, S5D**). After compiling the essential genes and tumor suppressive genes, we found that classical cancer signaling pathways may exert important functions in progression of hepatoblastoma, including the PI3K pathway (*Pten*), the p53 pathway (*Cdkn2a*, *Trp53*, *Myh9*, *Sox4*, *Dapk3*), and the RAS-RAF-MEK-mTOR pathway (*Grb2*, *Ptpn11*, *Kras*, *Raf*, *Map2k2*, *Mapk1*, *Rheb*, *mTor*, *Nf1*, *Lztr1*, *Rasa2*, *Dusp9*) (**Figure 5E**).

Genomic sequencing analysis of thousands of human tumors demonstrates that Hippo signaling pathway is widely dysregulated⁶², and plays a critical role in tumorigenesis of liver cancers¹⁸⁻²⁰. Our CRISPR screen identified key components of the Hippo pathway in hepatoblastoma (**Figure 5F**), including the oncogenic transcription factor YAP and its interaction partner TAZ, both of which are required for cancer cell survival. The tumor suppressive genes (*Tao1*, *Lats1*, *Nf2*), upstream of the Hippo pathway that inhibit YAP through phosphorylation-induced cytoplasmic retention and degradation, are important for hepatoblastoma proliferation. *Amotl2*, which encodes a Motin family member, Angiomotin-like 2, is a tumor suppressor that negatively regulates the YAP and TAZ function via AMOT-mediated tight junction localization⁶³. RhoA is a GTPase that controls YAP/TAZ translocation through promoting actin polymerization and stress fiber formation⁶⁴⁻⁶⁶. One study shows that RhoA–YAP–MYC signaling axis promotes the development of polycystic kidney disease⁶⁷. In summary, our genome-wide screen identified oncogenic pathways and targetable cancer dependency genes in our ABC-Myc hepatoblastoma model.

Murine and human hepatoblastoma share common essential and targetable genes

To determine if murine and human hepatoblastoma share common cancer dependency genes, we analyzed the essential genes identified through genome-wide CRISPR-Cas9 screen in HuH6, the human hepatoblastoma cell line included in the screening of a first-generation pediatric cancer dependency map⁶⁸. HuH6 bears *TP53* and *AXIN1* mutations (depmap.org). 963 essential genes (CRISPR score threshold -1.0) and 22 anti-proliferative genes (CRISPR score threshold 0.4) were identified in HuH6 cells (**Figure 5G, Table S7**). Pathway enrichment analysis showed that 963 essential genes are enriched with class 2 hepatoblastoma genes, targets of BMP2, DREAM complex, MYC and b-catenin (**Figure S6A**), all these pathways are commonly shared by the ABC-Myc cell line (**Figure 5D**). 52% of the essential genes in NEJF10 cells are shared by HuH6, including those targetable genes (i.e., *CDK7*, *CDK9*, *PRMT1*, *PRMT5*, *NEDD8*, *PLK1*) (**Figure 5G**), involved in a variety of biological functions (**Figure S6B**). Among the tumor suppressors, we found two (*NF2* and *PTEN*) are commonly shared between NEJF10 and HuH6 cells (**Figure 5H**). We identified several p53 pathway genes in NEJF10 cells. However, HuH6 has *TP53* mutation and therefore no selective pressure was conferred in the CRISPR screen. In summary, the oncogenic pathways and the therapeutically targetable genes are conserved both in our murine hepatoblastoma model and human hepatoblastoma.

Genetic mapping of chemotherapy response

Conventional chemotherapeutic agents (i.e., cisplatin, doxorubicin) play a critical role in hepatoblastoma treatment⁶⁹. These chemotherapeutic agents have significant toxicities and, in some cases, limited anti-

cancer efficacy. Thus, a better understanding of the genetic response of hepatoblastoma cells to chemotherapy may help to develop more effective and safer individual and combination therapies. To map the genetic response of chemotherapy, NEJF10 cells were transduced with a lentiviral pooled genome-wide sgRNA library and were divided into control and treatment groups (**Figure 6A**). Cells were treated with doxorubicin at two doses, IC₂₀ (5nM) and IC₉₀ (30nM) (**Figure S7A**), for 7 and 14 days, respectively. We identified hits whose mutation caused sensitization (negative selection) and resistance (positive selection) to doxorubicin. At the sublethal IC₂₀ dose, we identified 78 genes of negative selection (p<0.001, FDR<0.05) and 9 genes of positive selection (p<0.001, FDR<0.1) (**Figure 6B, Table S8**). However, at IC₉₀ dose, we only identified 70 positive selection genes (p<0.001, FDR<0.3) (**Figure 6D, Table S9**).

Functional protein association network analysis of negative selective genes at IC₂₀ revealed that most of them are physically and/or functionally connected, and function in DNA repair through non-homologous end-joining (NHEJ) (i.e., *Prkdc*, *Lig4*, *Xrcc4*) or homologous recombination (i.e., *Rad51*, *Rpa2*, *Xrcc2*), mitochondria (i.e., *Mtg2*, *Polg*, *Chchd3*), small nuclear RNA (snRNA) biogenesis through RNA polymerase II (i.e., *Ctu2*, *Snrnp40*, *Cstf1*), gene transcription (i.e., *Ints6*, *Ccnc*, *Asun*), and mitosis (i.e., *Aurka*, *Tpx2*) (**Figure 6C**). These data suggest that loss of function of NHEJ or homologous recombination mediated DNA repair may further worsen the DNA damage induced by doxorubicin, leading to enhanced cell death. *Prkdc*, which encodes DNA-PK to sense double strand DNA breaks and regulates DNA repair via NHEJ, has emerged as a new therapeutic target⁷⁰. Interestingly, disruption of a dozen of snRNA biogenesis genes also promoted the effect of doxorubicin. Notably, loss of function of *Aurka*, which encodes Aurora kinase A (AURKA) that is implicated in the regulation of cellular mitosis, led to enhanced effect of doxorubicin, consistent with recent studies showing that AURKA inhibitors potentiate the cancer cell killing of doxorubicin^{71,72}.

9 positive selection genes at IC₂₀ were obtained, including classical tumor suppressor genes such as *Cdkn2a*, *Pten*, *Trp53* (**Figure 6B**). As discussed above, *Dapk3* and *Sox4* are involved in regulation of the p53 pathway while *Lztr1* inhibits Ras activity (**Figure 5E**). *Rock2* and *Myl6* encode proteins functioning downstream of Rho GTPase activity⁷³. Although the mechanism of this pathway in chemoresistance remains to be investigated, one previous study showed that pharmacological inhibition of ROCK signaling enhances cisplatin resistance in neuroblastoma cells⁷⁴. *Wdr77*, encoding the non-catalytic component of the methylosome complex, composed of PRMT5, WDR77 and CLNS1A⁷⁵, has germ-line mutations in patients that predispose to familial papillary thyroid cancer⁷⁶. Transcriptome changes in pathways were enriched in the processes of cell cycle promotion and apoptosis in *WDR77* mutated tumors⁷⁶. These data indicate that loss of function of tumor suppressors blocks the effect of sublethal dose of doxorubicin. However, under the IC₉₀ lethal dose, the pathways conferring doxorubicin resistance were distinct from those under IC₂₀ dose selection (**Figure 6E**). In addition to the genes involved in

apoptosis, DNA replication and mitosis, the major components of these pathways are involved in regulation of homeostasis of RNA and protein, including pre-mRNA splicing (i.e., *Sf3b5*, *Hnrnpa1*, *Smu1*), protein translation and degradation (*Rpl7l1*, *Rpl3l*, *Psma1*, *Psma4*, *Cct5*) (**Figures 6E, F**). MAPK1, APAF1 and CASP9 are engaged in cytochrome C-mediated apoptotic response. *Faf1* encodes FAS-Associated Factor 1 (FAF1) that acts as a tumor suppressor by regulation of apoptosis and NF- κ B activity, and ubiquitination and proteasomal degradation⁷⁷. *Topors* encodes topoisomerase I-binding RING finger protein, which is a coactivator of p53 in growth suppression induced by DNA damage⁷⁸. While it is not surprising that inactivation of the apoptotic pathway leads to resistance to chemotherapy-mediated cancer killing, the mechanisms of RNA splicing and protein homeostasis in doxorubicin resistance are largely unknown. Nevertheless, these data provide a rationale to develop novel strategies to enhance efficacy of chemotherapy.

Drug screening using ABC-Myc-derived hepatoblastoma cells to identify new therapies

To develop a high-throughput screen platform using our ABC-Myc cell lines, we optimized the NEJF10 cell line in 384-well plate and treated cells with drugs currently being used for clinical cancer treatment, including 125 FDA-approved cancer drugs. With the range of 0.7-2 mM of tested compounds, 51 of them inhibited >50% of cell viability (**Figure S8A**), including conventional chemotherapeutic agents such as topoisomerase inhibitors, tubulin inhibitors, and nucleotide synthesis inhibitors (**Figure S8B**). We also found that ABC-Myc cells were sensitive to mTOR and MEK inhibitors, tyrosine kinase inhibitors, HDAC inhibitors and proteasome inhibitors, consistent with our CRISPR screening data showing that mTOR, EGFR, HDAC3, and proteasome are essential (**Table S5, S6**), indicating that these inhibitors may have clinical potential to treat hepatoblastoma patients. mTOR is activated downstream of YAP/TAZ in a YAP/b-catenin hepatoblastoma mouse model⁷⁹. mTOR inhibitors blocked hepatoblastoma growth in vitro and in xenograft models^{79,80}, and one clinical study showed that two hepatoblastoma patients treated with the mTOR inhibitor everolimus after liver transplantation did not develop any metastasis⁸¹. These data indicate that mTOR inhibition may be useful for treating hepatoblastoma patients especially for those who need liver transplantation, by benefiting from its anti-tumorigenic and immunosuppressive properties. One clinical study revealed that EGFR expression was elevated in hepatoblastoma specimens⁴⁹, as a target of the Wnt/b-catenin pathway in liver⁸², which may explain why ABC-Myc cell line is sensitive to genetic and pharmacologic inhibition of EGFR.

Our CRISPR screen revealed that *Cdk7* and *Aurka* were essential to ABC-Myc cells. Although the functions of CDK7 in hepatoblastoma have yet to be explored, CDK7 inhibition disrupts the transcriptional dependency of MYC-driven cancer⁸³. Several CDK7 inhibitors have been developed and two are in clinical trials (<https://clinicaltrials.gov/>). We treated five ABC-Myc cell lines with a selective CDK7 inhibitor, Samuraciclib⁸⁴, and found that this compound potently killed ABC-Myc cells

(IC₅₀<100nM) (**Figure S8C**). AURKA encodes aurora kinase A protein that is critical to G2/M phase progression during cell cycle. MYC and AURKA form a complex that represents for an actionable target in MYC-driven cancers^{85,86}. Indeed, in comparison with a primary human fibroblast cell line, the ABC-Myc cell lines were at least 100-fold more sensitive to the AURKA inhibitor, Alisertib (**Figure S8D**). These data indicate that ABC-Myc cell lines recapitulate the therapeutic vulnerability of human MYC-driven cancers. Our drug screening strategy allows the validation of the candidates obtained by the genomic screening through a different approach.

PRKDC inhibition enhances efficacy of chemotherapy

Loss of function of *Prkdc* synergized with doxorubicin effect in our CRISPR-Cas9 screen, providing a rationale to combine PRKDC inhibitors with chemotherapy to enhance efficacy. To validate the role of PRKDC, we used RNAi to knock down *Prkdc* in NEJF10 cells (**Figure 7A**), followed by doxorubicin treatment. Indeed, knockdown of *Prkdc* enhanced tumor cell killing by doxorubicin (**Figure 7B**). We then tested this hypothesis by treating NEJF10 cells with doxorubicin and a selective PRKDC inhibitor, AZD7648, which shows >90-fold cellular selectivity over its structurally related members ATM, ATR, and mTOR⁸⁷, and purity>99% (**Figure S9**). The colony formation assay demonstrated that AZD7648 synergized with doxorubicin to inhibit the cell survival of NEJF10 cells (**Figure 7C**). PrestoBlue assay with a BLISS index analysis further corroborated the synergistic effect of a PRKDC inhibitor and doxorubicin (**Figures 7D, S10A**). Annexin V staining followed by flow cytometry analysis showed that PRKDC inhibitor and doxorubicin combination induced greater apoptosis (**Figures S10B, S10C**). The synergistic effect of doxorubicin and AZD7648 was verified in additional ABC-Myc cell lines by colony formation assay (**Figure 7E**). We further validated the synergistic effect of doxorubicin and AZD7648 in HepG2 cells, a human hepatoblastoma cell line⁸⁸, and obtained similar results (**Figures 7F, S10D-F**). We then tested the combination therapy using our ABC-Myc mouse model. While monotherapy showed no benefit to ABC-Myc mice, the combination of AZD7648 and doxorubicin significantly extended mouse survival (**Figure 7G**), reducing the liver weight significantly, comparable to the normal liver weight (**Figure 7H**). In parallel, we tested the combination therapy using HepG2 xenografts. While doxorubicin showed modest anticancer effect, the combination of both led to a significant tumor growth delay in comparison with doxorubicin or AZD7648 alone (**Figures 7I, 7J**). In summary, the results from our CRISPR screen of the ABC-Myc model have identified therapeutic combinations that may be used in future clinical trials.

Discussion

Hepatocellular malignancies have become a leading cause of cancer-related deaths in people of all ages^{2,89,90}. Notably, the worldwide hepatoblastoma incidence has a greater rate of increase than other pediatric cancers². Surgical resection is critical for curing hepatoblastoma (HB), yet, unfortunately, two-thirds of patients have unresectable tumors at diagnosis⁶⁹, and so they need induction chemotherapy to enable surgical resection. Patients with resectable tumors have an event-free survival (EFS) of 80–90%

and can be cured with surgical resection combined with conventional chemotherapy⁶⁹. However, children with high-risk disease have poor outcomes with EFS survival under 50%^{50,69,91}. New therapeutic approaches for high-risk patients remain desperately needed. Unfortunately, lack of cell lines and animal models that resemble the high-risk human hepatoblastomas impedes our understanding of the pathogenesis of hepatoblastoma and identification of druggable targets. To meet the unmet clinical need, this study has (1) developed and validated the ABC-Myc hepatoblastoma model that closely resembles the histology of human hepatoblastoma and recapitulates the high-risk human disease at transcriptional levels, (2) generated ABC-Myc cell lines based upon the genetic model which are suitable for genome-wide genetic screen and high-throughput drug screens, (3) mapped the cancer dependency genes in ABC-Myc cells and defined the key oncogenic pathways that are shared by human hepatoblastoma cell lines, (4) identified the genetic modifiers of chemotherapy by a genome-wide CRISPR screen, (5) developed a combination therapy based upon the screening results that was translated to human hepatoblastoma models. Thus, this study has provided useful resources including disease models, targetable cancer dependency genes, and potentially more effective combination therapy approaches.

Previous approaches have been applied to establish hepatoblastoma models, including xenograft implantation^{92–100}, generation of transgenic mice^{28,48,101} and hydrodynamic tail vein injection of oncogenes^{22,24}, and each of these models has its pros and cons³⁴. Additionally, most of these models develop the well-differentiated fetal type of hepatoblastoma, which usually has a good clinical outcome even without chemotherapy administration¹⁰². In this study, we created a hepatocyte-specific transgenic c-Myc model, ABC-Myc, which rapidly develops multifocal hepatic neoplasms with pathological features of mixed fetal and embryonal hepatoblastoma, the most common histologic subtype in human disease. Molecular profiling demonstrates that the ABC-Myc hepatoblastoma resembles high-risk human disease, making this model uniquely useful for understanding the mechanisms of tumorigenesis and for testing therapy response in high-risk hepatoblastoma. Based on our ABC-Myc hepatoblastoma model, we generated cell lines that can be readily passaged *in vitro* in either 2D or 3D format. Using this line, we mapped the genome-wide cancer dependency genes of ABC-Myc hepatoblastoma and approximately 50% of these genes are also essential to HuH6 and HepG2, two human hepatoblastoma cell lines, suggesting that our ABC-Myc model and human hepatoblastomas share common oncogenic pathways. While hepatoblastoma lacks targetable somatic mutations, our screen identified numerous targetable genes including those encoding AURKA, CDK1, CDK7, CKD9, PLK1, PRMT1, PRMT5, EGFR and mTOR. The anticancer activity of inhibitors against AURKA, CDK7, mTOR and EGFR was validated *in vitro* in this study. While the clinical utility of drugging these targets with selective inhibitors awaits future testing, a PLK1 inhibitor, Volasertib, has shown anticancer activity in high-risk hepatoblastoma models¹⁰³. While genetic mutations in classical cancer pathways (i.e., CDKN2A-MDM2-p53, PTEN-PI3K-AKT-mTOR, Ras-Raf-MEK) are rare in primary hepatoblastomas at diagnosis, our screen results show that ABC-Myc tumor cells depend on them, suggesting that they may be dysregulated in other ways in hepatoblastoma and/or play important roles in cancer progression and relapsed disease. Particularly, we found that the Hippo signaling pathway is essential to ABC-Myc cell survival, in line with previous studies which demonstrate

that YAP1 and TAZ promote and maintain tumorigenesis of hepatoblastoma^{21,22,104}, supporting that our ABC-Myc model can be faithfully applied to identify hepatoblastoma-related oncogenic pathways. The roles of several tumor suppressive genes in hepatoblastoma identified from CRISPR screen are largely unknown. *Myh9*, which encodes nonmuscle myosin IIa, is a tumor suppressor in squamous cell carcinoma by regulating p53 stabilization¹⁰⁵. While the transcription factor SOX4 could be oncogenic, it also has tumor suppressive functions by modulating p53 function¹⁰⁶. Loss of function of *DAPK3* has been observed in several cancers¹⁰⁷, and DAPK3 regulates p53 activity by phosphorylating S20 on p53 to block MDM2-p53 interaction¹⁰⁸. DAPK3 also has kinase independent tumor suppressive function by driving tumor-intrinsic immunity through the STING-IFN β pathway¹⁰⁹. *Lzrt1* encodes leucine zipper-like transcriptional regulator 1 that is associated with RAS, functioning as an adaptor to promote RAS ubiquitination, thus inhibiting RAS oncogenic functions¹¹⁰. *Rasa2*, encoding a RasGAP to inhibit RAS activity, is a tumor-suppressor gene with loss-of-function in $\geq 30\%$ of human melanomas¹¹¹. DUSP9, a dual-specificity phosphatase, may exert its antitumor functions by suppressing mTOR pathway^{112,113}. The role of PAWR (Pro-Apoptotic WT1 Regulator) in cancer remains unknown and its antiproliferative activity might be due to its anti-apoptosis function¹¹⁴.

Adjuvant and neoadjuvant chemotherapy are the mainstays of hepatoblastoma treatment. Although chemotherapy intensification has resulted in improved outcomes for high-risk disease, this comes at the expense of significant ototoxicity and cardiotoxicity associated with cisplatin and doxorubicin. New combination therapies are badly needed to improve survival of patients. Using a genome-wide CRISPR screen, we have identified pathways whose loss-of-function enhance and antagonize the anti-tumor activity of doxorubicin. This has led to the identification of a more effective combination therapy in which a PRKDC inhibitor greatly enhances the efficacy of doxorubicin in ABC-Myc mice and human hepatoblastoma xenograft models. The advantage of our system is that we can test many different combinations based on screening of ABC-Myc cell lines *in vitro*, then validate the results in ABC-Myc mice *in vivo*, an approach not practical to carry out in clinical trials.

Methods

Generation of Alb-Cre;CAG-Myc (ABC-Myc) mice, and Alb-Cre;CAG-Myc;TdTomato (ABC-Myc; TdTomato) mice

Albumin-Cre (Alb-Cre) (Strain #003574), R26StopFLMYC (CAG-MYC) (Strain #020458), and CAG-tdTomato (Strain #007914) mice were obtained from the Jackson Laboratory. ABC-Myc (Alb-Cre^{+/wt}::CAG-MYC^{myc/wt}) mouse model was generated by crossbreeding Alb-Cre^{+/+} with CAG-MYC^{myc/myc} mouse, or Alb-Cre^{+/wt} with CAG-MYC^{myc/myc}, or Alb-Cre^{+/wt} with CAG-MYC^{myc/wt}. The littermates with genotypes of Alb-Cre^{wt/wt}::CAG-Myc^{myc/wt}, or Alb-Cre^{+/wt}::CAG-MYC^{wt/wt}, or Alb-Cre^{wt/wt}::CAG-MYC^{wt/wt} were served as normal controls. In order to generate ABC-MYC;TdTomato mice, Alb-Cre^{+/+} mice were first bred with CAG-Tdtomato^{td/td} mice to obtain the mice with genotypes of Alb-cre^{+/wt}::CAG-tdTomato^{td/wt}, which were then bred with CAG-Myc^{myc/myc} mice. For genotyping, the genomic DNA was extracted from

tail biopsies, and PCR amplification assay was performed using KAPA Mouse Genotyping Kits (Roche Corporate, Cat#KK7352) according to The Jackson Laboratory genotyping PCR conditions for each mice strain. The primers 5'-TGC AAA CAT CAC ATG CAC AC, GAA GCA GAA GCT TAG GAA GAT GG-3' and 5'-TTG GCC CCT TAC CAT AAC TG-3' were used for Alb-Cre genotyping (AlbCre = 390bp and WT = 351bp). The primers 5'-CCA AAG TCG CTC TGA GTT ATC-3', 5'-GAG CGG GAG AAA TGG ATA TG, CCA AGA GGG TCA AGT TGG A-3' and 5'-GCA ATA TGG TGG AAA ATA AC-3' are used for CAG-Myc genotyping (MYC = 550bp and WT = 604bp). The primers 5'-AAG GGA GCT GCA GTG GAG TA, CCG AAA ATC TGT GGG AAG TC-3', 5'-CTG TTC CTG TAC GGC ATG G-3' and 5'-GGC ATT AAA GCA GCG TAT CC-3' were used for CAG-tdTomato genotyping (tdTomato = 196 bp and WT = 297bp). The genotyping PCR products were resolved in 2% agarose gel (Invitrogen, Cat#16500-500) and imaged with Alphaimager HP (ProteinSimple, Alphaimager HP) or Li-COR D-Digit (Li-COR, 3500). Mice were housed with temperature and 12h light /12h dark cycle controlled under specific-pathogen-free conditions (SPF) at the St Jude Children's Research Hospital mouse facility. All experiments that involved the use of mice were performed in accordance with the guidelines outlined by the St Jude Children's Research Hospital Institutional Animal Care and Use Committee (IACUC).

Generation of ABC-Myc-derived hepatoblastoma cell lines (NEJF1, NEJF2, NEJF4, NEJF5, NEJF6)

The livers from ABC-Myc mice were excised and placed in a sterile tube containing phosphate-buffered saline (PBS) on wet ice during transport from the animal research facility to the research laboratory. Tumor nodules were excised using a sterile scalpel and underwent an enzymatic digestion with collagenase IV (2 mg/ml; in 25 ml of RPMI medium) for 1 hour in a 37°C rotor (Robbins Scientific Corporation, model 2000). After digestion, cells were filtered using a 70-µm sterile strainer and cultured in ultra-nonadherent cell culture plate with DMEM medium with 10% FBS and 1% penicillin and streptomycin. Liver cancer cells form spheroids and are propagated in ultra-nonadherent cell culture plate. In parallel, the spheroids were transferred to adherent plates in standard DMEM media and adherent cell lines were derived. Notably, the adherent cell lines form spheroids when culturing in non-adherent cell culture plate.

Generation of NEJF10 from the ABC-Myc;TdTOMATO tumor

The liver from ABC-Myc; TdTOMATO mouse (#NEJF10) was excised and placed in a sterile tube containing cold phosphate-buffered saline (PBS). Tumor nodules were excised using a sterile scalpel and underwent an enzymatic digestion with collagenase IV (2 mg/ml; in 25 ml of DMEM medium) for 1 hour in a 37°C rotor (Robbins Scientific Corporation, model 2000). After digestion, cells were filtered using a 70-µm sterile strainer and cultured in 15cm culture dish (Fisher Scientific, FB012925) with DMEM medium with 10% FBS and 1% penicillin and streptomycin. Next day, the NEJF10 hepatoblastoma cells formed spheroids with tdTomato red color under EVOS M7000 Imaging System (Invitrogen, EVOS M7000). The

spheroids were transferred and cultured in ultra-low attachment microplates for propagation (Corning, Cat#3471). The NEJF10 spheroids were transferred to adherent plates and the adherent NEJF10 cells were consequently derived. The adherent NEJF10 cells also form spheroids when cells were cultured back to ultra-low attachment microplates.

Human cell lines, reagents, and validation

HepG2 (ATCC, HB-8065) cells were cultured in 1X DMEM (Fisher Scientific, Cat#MT10013CM) supplemented with 10% FBS (Gibco, Cat#10437028), 1% Penicillin-Streptomycin solution (Gibco, Cat#15140122) at 37 °C in 5% CO₂ in a humidified incubator. All human-derived cell lines were validated by short tandem repeat (STR) profiling using PowerPlex® 16 HS System (Promega) once a month. Additionally, a polymerase chain reaction (PCR)-based method was used to screen for mycoplasma once a month employing the LookOut® Mycoplasma PCR Detection Kit (MP0035, Sigma-Aldrich) and JumpStart™ Taq DNA Polymerase (D9307, Sigma-Aldrich) to ensure cells were free of mycoplasma contamination.

Doxorubicin, Samuraciclib (ICEC0942), and EPZ015666 (GSK3235025) were purchased from Selleckchem. All other compounds used for screening were obtained from St Jude compounds deposit. AZD7648, Lot01, was purchased from Chemietek, and the quality was verified by Chemietek by HPLC-MS nad NMR, with purity >99.5%. The purity of AZD7648 was further verified in house by using Waters UPLC-MS system (Acquity PDA detector, SQ detector and UPLC BEH-C18 column). The mass spectrometer was acquired using MassLynx v. 4.1. The chromatographic conditions are as follows: flow rate: 1.0 mL/min, sample injection volume: 2 µL, column temperature: 55 °C, mobile phase: 0.1% formic acid in CH₃CN and H₂O.

Pathological assessment of ABC-Myc hepatoblastomas

Liver tumors were fixed in 10% neutral buffered formalin, embedded in paraffin, sectioned at 4 µm, mounted on positive charged glass slides (Superfrost Plus; 12-550-15, Thermo Fisher Scientific, Waltham, MA) that were dried at 60°C for 20 minutes, and stained with hematoxylin and eosin (HE). The following immunohistochemistry protocols were used for the detection of AFP, ARG1, Beta-catenin, GS, and KRT19, respectively, on commercial autostainers: 1) anti-Alpha-1-fetoprotein, A0008, Agilent, 1:300, 32' incubation. Heat-induced epitope retrieval, Cell conditioning media 2 (Ventana Medical Systems, Tucson, AZ), 32 minutes; Visualization with DISCOVERY OmniMap anti-Rb HRP (760-4311; Ventana Medical Systems), DISCOVERY ChromoMap DAB kit (760-159; Ventana Medical Systems). 2) anti-Arginase-1 (H-52), sc-20150, Santa Cruz, 1:75, 60' incubation. Heat-induced epitope retrieval, Cell conditioning media 2 (Ventana Medical Systems, Tucson, AZ), 48 minutes; Visualization with DISCOVERY OmniMap anti-Rb HRP (760-4311; Ventana Medical Systems), DISCOVERY ChromoMap DAB kit (760-159; Ventana Medical

Systems). 3) anti-Beta-catenin (Clone E247), RM-2101, ThermoFisher, 1:300, 60' incubation, Heat-induced epitope retrieval, Cell conditioning media 1 (Ventana Medical Systems, Tucson, AZ), 48 minutes. Visualization with DISCOVERY OmniMap anti-Rb HRP (760-4311; Ventana Medical Systems), DISCOVERY ChromoMap DAB kit (760-159; Ventana Medical Systems). 4) anti-Glutamine synthase, ab73593, Abcam, 1:1000, 60' incubation, Heat-induced epitope retrieval, Cell conditioning media 1 (Ventana Medical Systems, Tucson, AZ), 32 minutes. Visualization with DISCOVERY OmniMap anti-Rb HRP (760-4311; Ventana Medical Systems), DISCOVERY ChromoMap DAB kit (760-159; Ventana Medical Systems). 5) anti-Keratin19, TROMA-III, Developmental Studies Hybridoma bank, 1:1000, 15' incubation. Heat-induced epitope retrieval, Epitope Retrieval solution 1 (ER2), 20 minutes. Visualization with rabbit anti-rat (712-4126; Rockland), Bond Polymer Refine Detection (DS9800, Leica Biosystems). Additionally CD3, Galectin-2 (Mac-2), and VEGF were detected by IHC using the following autostainer protocols: 1) anti-CD3, sc-1127, SantaCruz, 1:1000, 32' incubation, heat-induced epitope retrieval with cell conditioning media 1 (Ventana Medical Systems, Tucson, AZ), 32 minutes; Visualization with Rabbit anti-goat IgG antibody (Vector labs, BA-5000) and DISCOVERY OmniMap anti-Rb HRP (760-4311; Ventana Medical Systems), DISCOVERY ChromoMap DAB kit (760-159; Ventana Medical Systems). 2) anti-Galectin-2 (Mac-2), M3/38, ACL8942AP, Accurate Chemical and Scientific Corporation, 1:1000, 32' incubation, heat-induced epitope retrieval with cell conditioning media 1 (Ventana Medical Systems, Tucson, AZ), 32 minutes; Visualization with DISCOVERY OmniMap anti-Rt HRP (760-4311; Ventana Medical Systems), DISCOVERY ChromoMap DAB kit (760-159; Ventana Medical Systems). 3) anti-VEGF, EP1176Y, NB110-57642, Novus, 1:100, 32' incubation, heat-induced epitope retrieval with cell conditioning media 1 (Ventana Medical Systems, Tucson, AZ), 32 minutes; Visualization with DISCOVERY OmniMap anti-Rb HRP (760-4311; Ventana Medical Systems), DISCOVERY ChromoMap DAB kit (760-159; Ventana Medical Systems). All HEs and IHCs were reviewed by light microscopy and interpreted by a board-certified veterinary pathologist (HT).

Clinical chemistry analysis

Once whole blood samples for chemistries are received in the Diagnostic Lab at St Jude, they are allowed to clot for 30 minutes, at which point the clot is removed and the serum separated by centrifuging at 5700 rpm for 10 minutes. Once separated, the serum is pipetted into a Horiba bio cup for processing. Data is processed on the Horiba Pentra 400 instrument and uploaded via the RSAS app directly into an excel spreadsheet for further analysis. The ABX Pentra chemistry panel reagents including ABX Pentra Albumin CP (REF# A11A01664), ABX Pentra ALP CP (REF# A11A01626), ABX Pentra ALT CP (REF# A11A01627), ABX Pentra Amylase CP (REF# A11A01628), ABX Pentra Urea CP (REF# A11A01641), ABX Pentra Calcium AS CP (REF# A11A01954), ABX Pentra Creatinine 120 CP (REF# A11A01933), ABX Pentra Glucose HK CP (REF# A11A01667), ABX Pentra Phosphorus CP (REF# A11A01665), ABX Pentra Potassium-E (REF# A11A01740), ABX Pentra Sodium-E (REF# A11A01738), ABX Pentra Bilirubin, Total CP (REF# A11A01639), ABX Pentra Total Protein 100 CP (REF# A11A01932), according to the manufacturer's instructions.

Complete blood counting

Once EDTA anti-coagulated samples for CBC's are received in the lab, they are immediately organized by ID number and processed on the Oxford Science hematology analyzer. The results are automatically downloaded onto an excel spreadsheet, reviewed by lab personnel and sent to the investigator via email for further analysis. In brief, blood was collected in Eppendorf tubes containing 10 µl of 10% EDTA via retroorbital bleed using 200 µl heparinized capillary tubes (Cat# 22-362-566, Fisher brand). Blood samples were processed within 2 h to avoid hemolysis. The number of leucocytes (WBC), erythrocytes (RBC), lymphocytes (LY), neutrophil (NE), monocytes (MO), eosinophils (EO) and platelets (PLT) were counted. Proprietary lysing agent was added to liberate hemoglobin and ultimately convert it to cyanmethemoglobin to calculate the value.

Western blot and antibodies

For western blotting, samples from normal livers and tumors excised from livers were homogenized with calculated volume of 2X sample buffer (1M TRIS/HCl, 10% SDS, 0.1% bromophenol-blue, 10% β-mercaptoethanol, 10% glycerol) and heated for 15 minutes at 95°C. Proteins were resolved on protein gels (Bio-Rad, Cat#4568083) and transferred onto PVDF membrane (Bio-Rad, Cat#170-4272) with Transblot Turbo transfer system (Bio-Rad, Cat#1704150). After being incubated with the primary antibody, horseradish peroxidase-(HRP) conjugated secondary antibody (Novex, Life technologies) at 1: 5000 was used for 1 hour incubation. The signals were detected by chemiluminescence (ECL, Thermo scientific). Images were taken with Li-COR Odyssey FC (Li-COR, Cat#2800). Antibodies including TD02 (Abclonal, A6766, RRID:AB_2767349, 1:1000), IDO2 (Mybiosource, MBS175296, 1:1000), C-MYC (Cell Signaling Technology, 5605S, RRID:AB_1903938, 1:1000), PRKDC (DNA-PK) (Novus, sc57-08, RRID: AB_2809479, 1:1000), b-actin (Sigma, A5441, RRID:AB_476744, 1:5000) and GAPDH-HRP (Cell Signaling Technology, 3683S, RRID:AB_1642205, 1:1000) were used for western blot.

Small interfering RNA Transfection and doxorubicin treatment

Small interfering RNAs (siRNA) were transfected into NEJF10 cells using Lipofectamine RNAiMax (Invitrogen, Cat#13778150) according to manufacturer's instructions. Non-Targeting siRNA#2 (Thermo Fisher Scientific, AM4637 <https://www.thermofisher.com/order/catalog/product/AM4637?SID=srch-hj-AM4637>) used as siRNA control. The siRNA oligos for Prkdc was ordered from Thermo Fisher Scientific (Thermo Fisher Scientific, AssayID151238, <https://www.thermofisher.com/order/genome-database/details/sirna/151238?CID=&ICID=&subtype=>, siRNA for mouse *Prkdc*:

Sense: 5-GGAAUUAUCUAUAGAUCCUTT-3; Antisense: 5-AGGAUCUAUAGUAUUAUCCTG-3). 72h hour post transfection, cells were harvested for western blot. For doxorubicin treatment experiments, 24h post siPrkdc transfection, cells were treated with doxorubicin with concentrations of 0, 15nM for 4 days and fixed with formaldehyde for crystal violet staining.

Bulk RNA-seq and analysis

Total stranded RNA sequencing data were processed by the internal AutoMapper pipeline. Briefly the raw reads were first trimmed (Trim-Galore version 0.60), mapped to mouse genome assembly (GRCm38, mm10) (STAR v2.7) and then the gene level values were quantified (RSEM v1.31) based on GENCODE annotation (VM22). Low count genes were removed from analysis using a CPM cutoff corresponding to a count of 10 reads and only confidently annotated (level 1 and 2 gene annotation) and protein-coding genes are used for differential expression analysis. Normalization factors were generated using the TMM method, counts were then transformed using voom and transformed counts were analyzed using the lmFit and eBayes functions (R limma package version 3.42.2). The significantly up- and down-regulated genes were defined by at least 2-fold changes and adjusted p-value < 0.05. Then Gene set enrichment analysis (GSEA) was carried out using gene-level log2 fold changes from differential expression results against gene sets in the Molecular Signatures Database (MSigDB 6.2) (gsea2 version 2.2.3).

Single-cell RNA-seq and analysis

Library preparation and sequencing. The liver tumor was harvested from ABC-Myc mouse. Tumor mass was dissociated by using a modified two-step collagenase procedure¹¹⁵. Briefly, the mouse was perfused with PBS containing 0.5mM EDTA and followed by perfusion with 2mg/ml of collagenase type IV (Worthington Biochemical Corporation, CLS-4) in DMEM (Dulbecco's Modified Eagle Medium) (Corning, 10-013-CM). The tumor from liver was chopped with razor and digested in 2mg/ml of collagenase type IV DMEM medium for 30 mins at 37°C. The cell suspension was filtered through a 70µm strainer and washed twice with DMEM. The dissociated cells were suspended in the DMEM medium. Before loaded into Chromium chips, cells were filtered again through a 40µm strainer and the single cells were counted by using a Luna cell counter, and then loaded into Chromium Chips V3 (10X Genomics) with a target capture of 8000 cells. The cDNA library construction and quality control were performed by following the manufacturer's protocol. The library was sequenced in Novaseq-V1 reagents. The sequenced data was processed by Cell Ranger Software (10X Genomics). *Data preprocessing.* UMIs mapped to genes encoding ribosomal/mitochondrial proteins were removed and cells with more than 40% of UMIs mapped to ribosomal/mitochondrial proteins were filtered. Cells with low (≤ 256 , potentially dead cells with broken membrane) or high ($\geq 32,768$, potentially two or more cells in a single droplet) UMI counts were further filtered. A total of 11,405 cells were captured with an average of 6,320 mRNA molecules (UMIs, median: 5,639, range: 343 – 32,747). The expression level of each gene is normalized to 10,000 UMIs per

cell and log transformed by adding 1 to the expression matrix. *Clustering*. The subpopulation structure of the whole dataset was inferred using Latent Cellular State Analysis (LCA), a novel clustering algorithm developed in house for analyzing large-scale scRNA-seq data¹¹⁶. Briefly, LCA first used singular value decomposition (SVD) to derive latent cellular states from the expression matrix for individual cells. Significant cellular states were determined using the Tracy-Widom test on eigenvalues. A modified version of spectral clustering was performed on the significant cellular states of individual cells (cellular states explained by potential technical variations including inter-sample difference and total UMIs were ignored) with different number of clusters (2-30). The optimal number of clusters was manually selected from top models determined by the silhouette measure for solutions with different number of clusters. *Data visualization*. Underneath cell variations were visualized in a 2D projection by t-distributed stochastic neighbor embedding (tSNE). Expression of individual genes or pathway scores were color coded (gray: not expressed; from low to high: blue-green-yellow-red) for each cell on tSNE plots. *Differentially expressed gene analysis*. Differentially expressed genes were analyzed by the negative binomial with independent dispersions¹¹⁷.

Spatiotranscriptomic analysis

Tissue harvest. The ABC-Myc mouse was anesthetized with avertin (0.8 ml/20 g of mouse body weight). The mouse chest cavity was opened to expose the heart with needles, tweezers, and dissecting scissors. The right auricle was incised, and the needle filled with PBS containing 0.5mM EDTA was immediately inserted into the apex of the left ventricle for the perfusion, followed by perfusion with 2mg/ml of collagenase type IV (Worthington Biochemical Corporation, CLS-4) in Dulbecco's Modified Eagle Medium (Fisher Scientific, Cat#MT10013CM). The tumor tissue was immediately isolated in the ice cold DMEM medium.

Pathological assessment. Fresh frozen tissues were sectioned and mounted on the ST Library preparation slides, HE stained, and scanned with a Zeiss Axioscan slide scanner to generate 20x digital whole slide images. CZI files were imported into HALO (v3.2.1851.351, Indica Labs) to annotate and classify bulky tissue regions as neoplasia, non-neoplastic hepatocytes and stroma, extramedullary hematopoiesis, glass/clear space, or tissue folds/artifacts based on morphology and tinctorial staining characteristics. *Tissue processing and data generation for spatial transcriptomics*. Flash frozen samples were embedded in OCT (Tissue-Tek, Sakura) and cryosectioned as per Tissue preparation guide from Visium Spatial Gene expression Kit- 10X Genomics (Cat.1000184). Briefly, the tumor tissue was harvested from ABC-MYC mouse liver in the ice cold DMEM medium (Fisher Scientific, Cat#MT10013CM), excess liquid was removed from tissue and flash frozen immediately in the bath of Isopentane and Liquid nitrogen. The OCT embedded tissue block was sectioned (10µm) and placed on the capture area of Visium Gene Expression Slide and stored at -80°C overnight. The tissue sections on the Visium slide were fixed with Methanol by incubating 30min at -20°C. The tissue was H&E stained following Visium Gene expression kit procedure. The H&E stained sections were imaged using AxioScan Z.1. Whole slide

scanner with standardized imaging protocol for Visium kit. After image acquisition, the slide sections were permeabilized for 18 min at 37°C and cDNA library was generated according to the Visium Spatial Gene Expression User Guide. The libraries were loaded and sequenced (R1-28cy, i7-10cy, i5-10cy and R2 -120 cycle) on Novaseq 6000 (Illumina) following recommendation of Visium Gene expression kit. The raw data was converted into FastQ and matrices of expression generated using the Space Range software V1.0 provided by 10X Genomics. *Data analysis.* Spatial transcriptome data were processed and visualized using R package Seurat. Data were normalized using sctransform recommended by Seurat. We also used Seurat's dimension reduction and clustering functionality to explore the spatial structures and patterns of gene expression. Expression patterns for chosen genes were visualized using feature plot function implemented in Seurat and ggplot2.

Annexin V/DAPI staining

Cells were seeded at a density of 100, 000 cells in each well in 6 well plates. Next day, cells were pretreated with AZD7648 for 1 h, before adding doxorubicin for further 48 h. Cells were trypsinized (0.05% trypsin for NEJF10 and 0.25% trypsin for HepG2) for 4 min and centrifuged at 1000 rpm for 5 min at 4 °C. Apoptosis was detected by dual staining of Annexin V-FITC and DAPI using apoptosis assay kit (TONBO biosciences, CA, USA) according to manufacturer's instructions. Annexin V-FITC/DAPI positive cells were Collected using log amplification, and 10,000 events were recorded (BD LSR-II, BD Biosciences, NJ, USA), and data was analyzed using BD FACSDiva™ Software.

NAD and NADH quantification

The levels of NAD and NADH were determined by using commercially NAD/NADH Quantification Colorimetric Kit (BioVision, Catalog # K337-100) according to the manufacturer's protocol. Briefly, the livers were excised from normal and ABC-Myc mice and placed in a sterile tube containing cold phosphate-buffered saline (PBS) in cold ice bucket during transport from the animal research facility to the research laboratory. About 20 mg of tumor nodules or normal liver tissues was homogenized in 400 µl of NAD/NADH extraction buffer in a micro-centrifuge tube and centrifuged at 14000 rpm at 4°C for 5 min. The extracted NAD/NADH supernatant was transferred into a new tube. Supernatants were divided to measure total NAD, (NADt = NAD + NADH) and NADH (by heating samples to 60 °C for 30 min to decompose NAD, while keeping NADH intact). Both NAD and NADH samples were mixed with NAD cycling enzyme and absorbance was measured at 450 nm with Synergy H1 microplate reader (BioTek, Synergy H1). Samples were always filtered with 10 K spin column (BioVision, Cat#1997) before performing the NAD/NADH quantification.

Crystal Violet Staining

ABC-Myc-derived hepatoblastoma cell lines (750 cells per well) and HepG2 (10,000 cells per well) cells were seeded in 6-well plates. After 24 hours, cells were treated with AZD7648 (0, 0.1, 0.33, 1 and 3.3 μ M). Doxorubicin (0, 7.5, 15, 30 and 60 nM for NEJF10 cell line and 0, 5, 25, 125 and 625 nM for HepG2) was added post AZD7648 treatment 1 hour. NEJF10 cell was cultured with DMEM complete medium for 5 days and HepG2 was cultured with DMEM complete medium for 8 days. The culture medium and AZD7648 and doxorubicin were changed every 2-3 days. After removing media, cells were washed with Dulbecco's phosphate buffered saline without calcium or magnesium (Lonza, Cat#17-516Q) and fixed with 4% formaldehyde in PBS for 20 minutes. Once formaldehyde was removed, cells were stained with 0.1% crystal violet (Sigma-Aldrich, Cat#HT90132-1L) for 1 hour. Plates were rinsed with water and imaged.

PrestoBlue assay and Bliss score calculation

PrestoBlue assay and Bliss score calculation was described as previous report (Alexandra et al., 2021) with minor modification. Briefly, NEJF10 (100 cells per well) and HepG2 (1000 cells per well) cells were seeded in 96-well plates. After 24 hours, cells were treated with AZD7648 (0, 0.1, 0.33, 1 and 3.3 μ M) and doxorubicin (0, 7.5, 15, 30 and 60 nM for NEJF10 cell line and 0, 5, 25, 125 and 625 nM for HepG2) in an 8x5 matrix. Cells were treated for 5 days, and cell viability was determined using the PrestoBlue assay (Invitrogen, A-13262) according to manufacturer's instructions. Cell viability for each treatment was normalized against the control group. A Bliss independence model was used to evaluate combination effects. Percentage over the Bliss score index was calculated with the equation (A+B)-AxB, in which A and B are the percentage of growth inhibitions induced by agents A and B at a given dose, respectively. The difference between the Bliss expectation and the observed growth inhibition induced by the combination of agent A and B at the same dose is the Bliss excess.

Cell viability assay for IC50 of CDK7 and AURKA inhibitors

Cell lines were plated in 384 well plates at 100 (NEJF1, NEJF10), 500 (NEJF2, NEJF4, NEJF6) or 1000 (CCLF_PEDS_0046_N), and treated with either samuraciclib or alisertib in technical quadruplicate at doses ranging from 2 nM to 20 μ M using a Tecan D300e compound printer (Tecan Biosciences). All wells were normalized to 0.1% total DMSO input. Cells were incubated at 37C until timepoint of assay development, using the Cell-Titer Glo assay (Promega). Data was processed using Graphpad Prism 7.0. Cell Lines: CCLF_PEDS_0046_N normal fibroblasts were a kind gift of the Cancer Cell Line Factory (Broad Institute, Cambridge, MA).

CRISPR screening for cancer dependency gene and genetic modifiers to doxorubicin

The Mouse CRISPR Knockout Pooled Library (Brie, lentiCRISPRv2) was obtained from Addgene (Addgene#73632), which includes 1000 control gRNAs and 78,637 gRNAs targeting 19,674 genes. The plasmid library was amplified and validated in the Center for Advanced Genome Engineering at St. Jude Children's Research Hospital as described in the Broad GPP protocol (<https://portals.broadinstitute.org/gpp/public/resources/protocols>) except EnduraTM DUOs (Lucigen) electrocompetent cells were used for the transformation step. The workflow of this whole genome genetic screen is illustrated in Figure 5A. We used NEJF-10 cells, a mouse hepatoblastoma cell line established in our laboratory by culturing dissociated liver mass cells from the ABC-Myc model. The cells were transduced with mouse CRISPR Knockout pooled library (Brie) which contains 78,637 unique sgRNA sequences targeting 19,674 human genes (4 sgRNAs per gene, and 1000 non-targeting controls) at a low MOI (~0.3) to ensure effective barcoding of individual cells. Cells were replenished with fresh DMEM medium containing 2 µg/mL puromycin (Millipore Sigma) for 36 h. After puromycin selection, cells were washed to eliminate dead cell debris and maintained in complete DMEM medium, and 32x 10⁶ cells were collected for genomic DNA extraction to ensure over 400× coverage of Brie library. The transduced cells were cultured for 5 days for CRISPR editing to generate a mutant cell pool, which was then treated with vehicle (DMSO) and doxorubicin (IC20~5 nM, 14 days; IC90~30nM 21 days), these concentrations were selected from colony formation assay that mimics similar experimental setup for actual experiment (IC20~7.8 n M, IC90~125 nM, for 3 days). During the experiment, at least 32x 10⁶ cells were collected for genomic DNA extraction to ensure over 400× coverage of Brie library. The total genomic DNA was extracted using a DNeasy Blood & Tissue Kit (Qiagen) and quantified with a Nanodrop instrument. The sgRNA sequences were amplified using PCR method using NEB Q5 polymerase (New England Biolabs). PCR products were purified by AMPure XP SPRI beads (Beckman Coulter) and quantified by a Qubit dsDNA HS assay (Thermo Fisher Scientific). A total of 16 million reads were sequenced using an Illumina HiSeq sequencer, and the sequencing data were analyzed using MAGeCK-VISPR software. NGS sequencing was performed in the Hartwell Center Genome Sequencing Facility at St. Jude Children's Research Hospital. Single-end, 100-cycle sequencing was performed on a NovaSeq 6000 (Illumina). Validation to check gRNA presence and representation was performed using calc_auc_v1.1.py (<https://github.com/mhegde/>) and count_spacers.py.

Drug response screen

For the screen, assay-ready plates were prepared by dispensing 50nl small molecules in empty white 384-well plates (Corning) using Echo 555 Liquid Handler (Labcyte). 50µl ABC-Myc cells per well were seeded in the assay-ready plates. The cells were incubated at 37°C, 5% CO₂ in a humidified cell culture incubator (LiCONiC) for five days. Prior to the cytotoxicity assay, 25µl medium per well was removed by Apricot S2 (SPT Labtech). To quantify the cytotoxicity, the amount of intracellular ATP was measured by CellTiter Glo (Promega). Widget, an automated robot system in St. Jude Children's Research Hospital was utilized for the cytotoxicity assay. 25µl CellTiter Glo reagent (Promega) was added to each well by Multidrop Combi (ThermoFisher). After shaking plates, plates were incubated for 20 minutes at room temperature.

Then, the luminescent signal was measured by EnVision (PerkinElmer). Luminescent signal results were analyzed by Genedata Screener (Genedata). All the results were normalized by the negative control (DMSO) and the positive control (5 μ M 17-DMAG).

In vivo therapy

(1) Transgenic ABC-Myc mice mouse model. All the animals are procured at Animal Resource Center (ARC) at St. Jude Children's Research Hospital and study was approved by Institutional Animal Care and Use Committee. Following genotyping, ABC-Myc mice were randomized and assigned to treatment groups. Inclusion criteria were the presence of the ABC-Myc allele, either in heterozygosity or both ABC-Myc alleles, age ranging 16-18 days after birth, both genders. Mice were treated with vehicle, doxorubicin (0.75 mg/kg, intraperitoneal, twice weekly) and AZD7648 (50 mg/kg/day, twice, oral gavage, everyday); either agent alone or in combination with doxorubicin and AZD7648 for three weeks. The mice weight and activity were monitored throughout the experiment. The humane end point was decided (notified by staff not directly involved in this study) to euthanize the mice. The livers from treatment groups of ABC-Myc mice and age matching normal mice were excised, weighed and imaged. (2) HepG2 xenograft study. 4–6-week-old female NSG mice (NOD.Cg-Prkdc scid Il2rg tm1Wjl /SzJ) were housed in pathogen-free conditions with food and water provided ad libitum. HepG2 cells (5×10^6 /mouse) in 100 μ l PBS were injected subcutaneously on the right flank of mice. When the tumor size reached up to ~100 mm³, the animals were randomized into four groups (n=5 mice per group). Mice were treated with vehicle, doxorubicin (1 mg/kg, intraperitoneal, twice weekly) and AZD7648 (50 mg/kg/day, oral gavage everyday); either agent alone or in combination with doxorubicin and AZD7648 for three weeks. The tumor volume and mice weight were measured twice in a week. All the mice were euthanized, and subcutaneous tumors were collected, imaged and weighed. The tumor volume and weight were presented as the means \pm S.D (n = 5). In vivo studies were approved and conducted in accordance with Institutional Animal Care and Use Committee at St. Jude Children's Research Hospital.

Declarations

Data availability

Bulk RNA-seq GEO accession number of this SuperSeries: **GSE193124**

Link for reviewer access: <https://www.ncbi.nlm.nih.gov/geo/query/acc.cgi?acc=GSE193124&token=cdenicyllahbyn>

scRNA-seq and spatiotranscriptomics GEO accession number of this SuperSeries: **GSE195575, GSE194051**

To review GEO accession GSE195575: Go to <https://www.ncbi.nlm.nih.gov/geo/query/acc.cgi?acc=GSE195575>

Enter token mfufqkgwtvczpmdu into the box

To review GEO accession GSE194051: Go to

<https://www.ncbi.nlm.nih.gov/geo/query/acc.cgi?acc=GSE194051>

Enter token ilofqgeazjcbxyp into the box

Acknowledgments. We thank the staff of the St. Jude Animal Resource Center, Hartwell Center and Applied Center for Bioinformatics for their dedication and expertise. The work was supported by American Cancer Society-Research Scholar (130421-RSG-17-071-01-TBG, J.Y.), National Cancer Institute (1R01CA229739-01, J.Y.). The content is solely the responsibility of the authors and does not necessarily represent the official views of the National Institutes of Health.

Author Contribution: **J. Yang:** Conceptualization, data curation, formal analysis, supervision, validation, investigation, visualization, methodology, writing-original draft, writing-review and editing. **X. Chen:** Conceptualization, data curation, formal analysis, supervision, validation, investigation, visualization, methodology, writing-review and editing. **J. Fang, S. Singh, S. Natarajan, H. Tillman, A. Durbin, HW. Lee, C. Cheng, W. Chen, H. Jin, W. Chen, J. Rehg:** Data curation, formal analysis, validation, investigation, visualization, methodology, writing-review and editing. **A. Abu-Zaid, J. Steele, J. Connelly, Y. Wang, S. Cairo:** Formal analysis, methodology, writing-review and editing. **Q. Wu:** validation, methodology. **Y. Fan, S. Pruett-Miller, T. Chen, J. Easton:** Supervision, methodology, writing-review and editing. **R. Wang, E. Glazer, A. Murphy:** Conceptualization, writing-review and editing. **A. Davidoff:** Conceptualization, supervision, writing-review and editing.

References

1. Lau, C. S., Mahendaraj, K. & Chamberlain, R. S. Hepatocellular Carcinoma in the Pediatric Population: A Population Based Clinical Outcomes Study Involving 257 Patients from the Surveillance, Epidemiology, and End Result (SEER) Database (1973–2011). *HPB Surg* 2015, 670728, doi:10.1155/2015/670728 (2015).

2. Hubbard, A. K., Spector, L. G., Fortuna, G., Marcotte, E. L. & Poynter, J. N. Trends in International Incidence of Pediatric Cancers in Children Under 5 Years of Age: 1988–2012. *JNCI Cancer Spectr* **3**, pkz007, doi:10.1093/jncics/pkz007 (2019).
3. Spector, L. G. & Birch, J. The epidemiology of hepatoblastoma. *Pediatr Blood Cancer* **59**, 776–779, doi:10.1002/pbc.24215 (2012).
4. Schady, D. A., Roy, A. & Finegold, M. J. Liver tumors in children with metabolic disorders. *Transl Pediatr* **4**, 290–303, doi:10.3978/j.issn.2224-4336.2015.10.08 (2015).
5. Lim, I. I. P., Bondoc, A. J., Geller, J. I. & Tiao, G. M. Hepatoblastoma-The Evolution of Biology, Surgery, and Transplantation. *Children (Basel)* **6**, doi:10.3390/children6010001 (2018).
6. Grobner, S. N. *et al.* The landscape of genomic alterations across childhood cancers. *Nature* **555**, 321–327, doi:10.1038/nature25480 (2018).
7. Tomlinson, G. E. & Kappler, R. Genetics and epigenetics of hepatoblastoma. *Pediatr Blood Cancer* **59**, 785–792, doi:10.1002/pbc.24213 (2012).
8. Zhang, Y. *et al.* Molecular Mechanisms of Hepatoblastoma. *Semin Liver Dis* **41**, 28–41, doi:10.1055/s-0040-1722645 (2021).
9. Sumazin, P. *et al.* Genomic analysis of hepatoblastoma identifies distinct molecular and prognostic subgroups. *Hepatology* **65**, 104–121, doi:10.1002/hep.28888 (2017).
10. Eichenmuller, M. *et al.* The genomic landscape of hepatoblastoma and their progenies with HCC-like features. *J Hepatol* **61**, 1312–1320, doi:10.1016/j.jhep.2014.08.009 (2014).
11. Cairo, S. *et al.* Hepatic stem-like phenotype and interplay of Wnt/beta-catenin and Myc signaling in aggressive childhood liver cancer. *Cancer Cell* **14**, 471–484, doi:10.1016/j.ccr.2008.11.002 (2008).
12. Jia, D. *et al.* Exome sequencing of hepatoblastoma reveals novel mutations and cancer genes in the Wnt pathway and ubiquitin ligase complex. *Hepatology* **60**, 1686–1696, doi:10.1002/hep.27243 (2014).
13. Buendia, M. A. Unravelling the genetics of hepatoblastoma: few mutations, what else? *J Hepatol* **61**, 1202–1204, doi:10.1016/j.jhep.2014.09.016 (2014).
14. Sekiguchi, M. *et al.* Integrated multiomics analysis of hepatoblastoma unravels its heterogeneity and provides novel druggable targets. *NPJ Precis Oncol* **4**, 20, doi:10.1038/s41698-020-0125-y (2020).
15. Carrillo-Reixach, J. *et al.* Epigenetic footprint enables molecular risk stratification of hepatoblastoma with clinical implications. *J Hepatol* **73**, 328–341, doi:10.1016/j.jhep.2020.03.025 (2020).
16. Nagae, G. *et al.* Genetic and epigenetic basis of hepatoblastoma diversity. *Nat Commun* **12**, 5423, doi:10.1038/s41467-021-25430-9 (2021).
17. Hirsch, T. Z. *et al.* Integrated Genomic Analysis Identifies Driver Genes and Cisplatin-Resistant Progenitor Phenotype in Pediatric Liver Cancer. *Cancer Discov* **11**, 2524–2543, doi:10.1158/2159-8290.CD-20-1809 (2021).
18. Mo, J. S., Park, H. W. & Guan, K. L. The Hippo signaling pathway in stem cell biology and cancer. *EMBO Rep* **15**, 642–656, doi:10.15252/embr.201438638 (2014).

19. Moya, I. M. & Halder, G. Hippo-YAP/TAZ signalling in organ regeneration and regenerative medicine. *Nat Rev Mol Cell Biol* **20**, 211–226, doi:10.1038/s41580-018-0086-y (2019).
20. Patel, S. H., Camargo, F. D. & Yimlamai, D. Hippo Signaling in the Liver Regulates Organ Size, Cell Fate, and Carcinogenesis. *Gastroenterology* **152**, 533–545, doi:10.1053/j.gastro.2016.10.047 (2017).
21. Smith, J. L. *et al.* YAP1 Withdrawal in Hepatoblastoma Drives Therapeutic Differentiation of Tumor Cells to Functional Hepatocyte-Like Cells. *Hepatology* **73**, 1011–1027, doi:10.1002/hep.31389 (2021).
22. Tao, J. *et al.* Activation of beta-catenin and Yap1 in human hepatoblastoma and induction of hepatocarcinogenesis in mice. *Gastroenterology* **147**, 690–701, doi:10.1053/j.gastro.2014.05.004 (2014).
23. Zhang, J. *et al.* TEA Domain Transcription Factor 4 Is the Major Mediator of Yes-Associated Protein Oncogenic Activity in Mouse and Human Hepatoblastoma. *Am J Pathol* **189**, 1077–1090, doi:10.1016/j.ajpath.2019.01.016 (2019).
24. Min, Q. *et al.* beta-Catenin and Yes-Associated Protein 1 Cooperate in Hepatoblastoma Pathogenesis. *Am J Pathol* **189**, 1091–1104, doi:10.1016/j.ajpath.2019.02.002 (2019).
25. Sylvester, K. G. & Colnot, S. Hippo/YAP, beta-catenin, and the cancer cell: a "menage a trois" in hepatoblastoma. *Gastroenterology* **147**, 562–565, doi:10.1053/j.gastro.2014.07.026 (2014).
26. Cairo, S., Armengol, C. & Buendia, M. A. Activation of Wnt and Myc signaling in hepatoblastoma. *Front Biosci (Elite Ed)* **4**, 480–486, doi:10.2741/393 (2012).
27. Wang, H. *et al.* Coordinated Activities of Multiple Myc-dependent and Myc-independent Biosynthetic Pathways in Hepatoblastoma. *J Biol Chem* **291**, 26241–26251, doi:10.1074/jbc.M116.754218 (2016).
28. Comerford, S. A. *et al.* Hepatoblastoma modeling in mice places Nrf2 within a cancer field established by mutant beta-catenin. *JCI Insight* **1**, e88549, doi:10.1172/jci.insight.88549 (2016).
29. Zhang, W. *et al.* beta-Catenin mutations as determinants of hepatoblastoma phenotypes in mice. *J Biol Chem* **294**, 17524–17542, doi:10.1074/jbc.RA119.009979 (2019).
30. Cairo, S. *et al.* Stem cell-like micro-RNA signature driven by Myc in aggressive liver cancer. *Proc Natl Acad Sci U S A* **107**, 20471–20476, doi:10.1073/pnas.1009009107 (2010).
31. Weber, R. G., Pietsch, T., von Schweinitz, D. & Lichter, P. Characterization of genomic alterations in hepatoblastomas. A role for gains on chromosomes 8q and 20 as predictors of poor outcome. *Am J Pathol* **157**, 571–578, doi:10.1016/S0002-9440(10)64567-1 (2000).
32. Tomlinson, G. E. Cytogenetics of hepatoblastoma. *Front Biosci (Elite Ed)* **4**, 1287–1292, doi:10.2741/459 (2012).
33. Rikhi, R. R. *et al.* Hepatoblastoma: A Need for Cell Lines and Tissue Banks to Develop Targeted Drug Therapies. *Front Pediatr* **4**, 22, doi:10.3389/fped.2016.00022 (2016).
34. Whitlock, R. S., Yang, T., Vasudevan, S. A. & Woodfield, S. E. Animal Modeling of Pediatric Liver Cancer. *Cancers (Basel)* **12**, doi:10.3390/cancers12020273 (2020).

35. Postic, C. *et al.* Dual roles for glucokinase in glucose homeostasis as determined by liver and pancreatic beta cell-specific gene knock-outs using Cre recombinase. *J Biol Chem* **274**, 305–315, doi:10.1074/jbc.274.1.305 (1999).
36. Calado, D. P. *et al.* The cell-cycle regulator c-Myc is essential for the formation and maintenance of germinal centers. *Nat Immunol* **13**, 1092–1100, doi:10.1038/ni.2418 (2012).
37. Lopez-Terrada, D. *et al.* Towards an international pediatric liver tumor consensus classification: proceedings of the Los Angeles COG liver tumors symposium. *Mod Pathol* **27**, 472–491, doi:10.1038/modpathol.2013.80 (2014).
38. Ranganathan, S., Lopez-Terrada, D. & Alaggio, R. Hepatoblastoma and Pediatric Hepatocellular Carcinoma: An Update. *Pediatr Dev Pathol*, 1093526619875228, doi:10.1177/1093526619875228 (2019).
39. Yan, B. C. *et al.* Arginase-1: a new immunohistochemical marker of hepatocytes and hepatocellular neoplasms. *Am J Surg Pathol* **34**, 1147–1154, doi:10.1097/PAS.0b013e3181e5dff (2010).
40. Gong, A. & Huang, S. FoxM1 and Wnt/beta-catenin signaling in glioma stem cells. *Cancer Res* **72**, 5658–5662, doi:10.1158/0008-5472.CAN-12-0953 (2012).
41. Wang, J. D. *et al.* Pediatric liver tumors: initial presentation, image finding and outcome. *Pediatr Int* **49**, 491–496, doi:10.1111/j.1442-200X.2007.02384.x (2007).
42. Hsiao, C. C., Chuang, J. H., Tiao, M. M., Sheen, J. M. & Shieh, C. S. Patterns of hepatoblastoma and hepatocellular carcinoma in children after universal hepatitis B vaccination in taiwan: a report from a single institution in southern Taiwan. *J Pediatr Hematol Oncol* **31**, 91–96, doi:10.1097 MPH.0b013e31818b3784 (2009).
43. Subramanian, A. *et al.* Gene set enrichment analysis: a knowledge-based approach for interpreting genome-wide expression profiles. *Proc Natl Acad Sci U S A* **102**, 15545–15550, doi:10.1073/pnas.0506580102 (2005).
44. Chiang, D. Y. *et al.* Focal gains of VEGFA and molecular classification of hepatocellular carcinoma. *Cancer Res* **68**, 6779–6788, doi:10.1158/0008-5472.CAN-08-0742 (2008).
45. Lee, J. S. *et al.* Application of comparative functional genomics to identify best-fit mouse models to study human cancer. *Nat Genet* **36**, 1306–1311, doi:10.1038/ng1481 (2004).
46. Servitja, J. M. *et al.* Hnf1alpha (MODY3) controls tissue-specific transcriptional programs and exerts opposed effects on cell growth in pancreatic islets and liver. *Mol Cell Biol* **29**, 2945–2959, doi:10.1128/MCB.01389-08 (2009).
47. Hooks, K. B. *et al.* New insights into diagnosis and therapeutic options for proliferative hepatoblastoma. *Hepatology* **68**, 89–102, doi:10.1002/hep.29672 (2018).
48. Nguyen, L. H. *et al.* Lin28b is sufficient to drive liver cancer and necessary for its maintenance in murine models. *Cancer Cell* **26**, 248–261, doi:10.1016/j.ccr.2014.06.018 (2014).
49. Lopez-Terrada, D. *et al.* Histologic subtypes of hepatoblastoma are characterized by differential canonical Wnt and Notch pathway activation in DLK + precursors. *Hum Pathol* **40**, 783–794, doi:10.1016/j.humpath.2008.07.022 (2009).

50. Perilongo, G. *et al.* Hepatoblastoma presenting with lung metastases: treatment results of the first cooperative, prospective study of the International Society of Paediatric Oncology on childhood liver tumors. *Cancer* **89**, 1845–1853, doi:10.1002/1097-0142(20001015)89:8<1845::aid-cncr27>3.0.co;2-d (2000).
51. Platten, M., Nollen, E. A. A., Rohrig, U. F., Fallarino, F. & Opitz, C. A. Tryptophan metabolism as a common therapeutic target in cancer, neurodegeneration and beyond. *Nat Rev Drug Discov* **18**, 379–401, doi:10.1038/s41573-019-0016-5 (2019).
52. Tummala, K. S. *et al.* Inhibition of de novo NAD(+) synthesis by oncogenic URI causes liver tumorigenesis through DNA damage. *Cancer Cell* **26**, 826–839, doi:10.1016/j.ccr.2014.10.002 (2014).
53. MacParland, S. A. *et al.* Single cell RNA sequencing of human liver reveals distinct intrahepatic macrophage populations. *Nat Commun* **9**, 4383, doi:10.1038/s41467-018-06318-7 (2018).
54. Su, X. *et al.* Single-cell RNA-Seq analysis reveals dynamic trajectories during mouse liver development. *BMC Genomics* **18**, 946, doi:10.1186/s12864-017-4342-x (2017).
55. Segal, J. M. *et al.* Single cell analysis of human foetal liver captures the transcriptional profile of hepatobiliary hybrid progenitors. *Nat Commun* **10**, 3350, doi:10.1038/s41467-019-11266-x (2019).
56. Jungermann, K. & Kietzmann, T. Zonation of parenchymal and nonparenchymal metabolism in liver. *Annu Rev Nutr* **16**, 179–203, doi:10.1146/annurev.nu.16.070196.001143 (1996).
57. Kietzmann, T. Metabolic zonation of the liver: The oxygen gradient revisited. *Redox Biol* **11**, 622–630, doi:10.1016/j.redox.2017.01.012 (2017).
58. Halpern, K. B. *et al.* Single-cell spatial reconstruction reveals global division of labour in the mammalian liver. *Nature* **542**, 352–356, doi:10.1038/nature21065 (2017).
59. Massalha, H. *et al.* A single cell atlas of the human liver tumor microenvironment. *Mol Syst Biol* **16**, e9682, doi:10.15252/msb.20209682 (2020).
60. Zhang, Q. *et al.* Landscape and Dynamics of Single Immune Cells in Hepatocellular Carcinoma. *Cell* **179**, 829–845 e820, doi:10.1016/j.cell.2019.10.003 (2019).
61. Pfister, S. M. *et al.* A Summary of the Inaugural WHO Classification of Pediatric Tumors: Transitioning from the Optical into the Molecular Era. *Cancer Discov* **12**, 331–355, doi:10.1158/2159-8290.CD-21-1094 (2022).
62. Wang, Y. *et al.* Comprehensive Molecular Characterization of the Hippo Signaling Pathway in Cancer. *Cell Rep* **25**, 1304–1317 e1305, doi:10.1016/j.celrep.2018.10.001 (2018).
63. Zhao, B. *et al.* Angiomotin is a novel Hippo pathway component that inhibits YAP oncoprotein. *Genes Dev* **25**, 51–63, doi:10.1101/gad.2000111 (2011).
64. Wada, K., Itoga, K., Okano, T., Yonemura, S. & Sasaki, H. Hippo pathway regulation by cell morphology and stress fibers. *Development* **138**, 3907–3914, doi:10.1242/dev.070987 (2011).
65. Aragona, M. *et al.* A mechanical checkpoint controls multicellular growth through YAP/TAZ regulation by actin-processing factors. *Cell* **154**, 1047–1059, doi:10.1016/j.cell.2013.07.042 (2013).

66. Dupont, S. *et al.* Role of YAP/TAZ in mechanotransduction. *Nature* **474**, 179–183, doi:10.1038/nature10137 (2011).
67. Cai, J. *et al.* A RhoA-YAP-c-Myc signaling axis promotes the development of polycystic kidney disease. *Genes Dev* **32**, 781–793, doi:10.1101/gad.315127.118 (2018).
68. Dharia, N. V. *et al.* A first-generation pediatric cancer dependency map. *Nat Genet* **53**, 529–538, doi:10.1038/s41588-021-00819-w (2021).
69. Trobaugh-Lotrario, A. D. & Katzenstein, H. M. Chemotherapeutic approaches for newly diagnosed hepatoblastoma: past, present, and future strategies. *Pediatr Blood Cancer* **59**, 809–812, doi:10.1002/pbc.24219 (2012).
70. Blackford, A. N. & Jackson, S. P. ATM, ATR, and DNA-PK: The Trinity at the Heart of the DNA Damage Response. *Mol Cell* **66**, 801–817, doi:10.1016/j.molcel.2017.05.015 (2017).
71. Borges, K. S. *et al.* The aurora kinase inhibitor AMG 900 increases apoptosis and induces chemosensitivity to anticancer drugs in the NCI-H295 adrenocortical carcinoma cell line. *Anticancer Drugs* **28**, 634–644, doi:10.1097/CAD.0000000000000504 (2017).
72. Kamran, M. *et al.* Aurora kinase A regulates Survivin stability through targeting FBXL7 in gastric cancer drug resistance and prognosis. *Oncogenesis* **6**, e298, doi:10.1038/oncsis.2016.80 (2017).
73. Hartmann, S., Ridley, A. J. & Lutz, S. The Function of Rho-Associated Kinases ROCK1 and ROCK2 in the Pathogenesis of Cardiovascular Disease. *Front Pharmacol* **6**, 276, doi:10.3389/fphar.2015.00276 (2015).
74. Street, C. A. *et al.* Pharmacological inhibition of Rho-kinase (ROCK) signaling enhances cisplatin resistance in neuroblastoma cells. *Int J Oncol* **37**, 1297–1305, doi:10.3892/ijo_00000781 (2010).
75. Friesen, W. J. *et al.* A novel WD repeat protein component of the methylosome binds Sm proteins. *J Biol Chem* **277**, 8243–8247, doi:10.1074/jbc.M109984200 (2002).
76. Zhao, Y. *et al.* Germ-line mutations in WDR77 predispose to familial papillary thyroid cancer. *Proc Natl Acad Sci U S A* **118**, doi:10.1073/pnas.2026327118 (2021).
77. Menges, C. W., Altomare, D. A. & Testa, J. R. FAS-associated factor 1 (FAF1): diverse functions and implications for oncogenesis. *Cell Cycle* **8**, 2528–2534, doi:10.4161/cc.8.16.9280 (2009).
78. Lin, L. *et al.* topors, a p53 and topoisomerase I-binding RING finger protein, is a coactivator of p53 in growth suppression induced by DNA damage. *Oncogene* **24**, 3385–3396, doi:10.1038/sj.onc.1208554 (2005).
79. Liu, P. *et al.* Central role of mTORC1 downstream of YAP/TAZ in hepatoblastoma development. *Oncotarget* **8**, 73433–73447, doi:10.18632/oncotarget.20622 (2017).
80. Wagner, F. *et al.* Rapamycin blocks hepatoblastoma growth in vitro and in vivo implicating new treatment options in high-risk patients. *Eur J Cancer* **48**, 2442–2450, doi:10.1016/j.ejca.2011.12.032 (2012).
81. Nielsen, D. *et al.* The use of everolimus in pediatric liver transplant recipients: first experience in a single center. *Pediatr Transplant* **15**, 510–514, doi:10.1111/j.1399-3046.2011.01515.x (2011).

82. Tan, X. *et al.* Epidermal growth factor receptor: a novel target of the Wnt/beta-catenin pathway in liver. *Gastroenterology* **129**, 285–302, doi:10.1053/j.gastro.2005.04.013 (2005).
83. Chipumuro, E. *et al.* CDK7 inhibition suppresses super-enhancer-linked oncogenic transcription in MYCN-driven cancer. *Cell* **159**, 1126–1139, doi:10.1016/j.cell.2014.10.024 (2014).
84. Patel, H. *et al.* ICEC0942, an Orally Bioavailable Selective Inhibitor of CDK7 for Cancer Treatment. *Mol Cancer Ther* **17**, 1156–1166, doi:10.1158/1535-7163.MCT-16-0847 (2018).
85. Dauch, D. *et al.* A MYC-aurora kinase A protein complex represents an actionable drug target in p53-altered liver cancer. *Nat Med* **22**, 744–753, doi:10.1038/nm.4107 (2016).
86. Otto, T. *et al.* Stabilization of N-Myc is a critical function of Aurora A in human neuroblastoma. *Cancer Cell* **15**, 67–78, doi:10.1016/j.ccr.2008.12.005 (2009).
87. Fok, J. H. L. *et al.* AZD7648 is a potent and selective DNA-PK inhibitor that enhances radiation, chemotherapy and olaparib activity. *Nat Commun* **10**, 5065, doi:10.1038/s41467-019-12836-9 (2019).
88. Lopez-Terrada, D., Cheung, S. W., Finegold, M. J. & Knowles, B. B. Hep G2 is a hepatoblastoma-derived cell line. *Hum Pathol* **40**, 1512–1515, doi:10.1016/j.humpath.2009.07.003 (2009).
89. Global Burden of Disease Liver Cancer, C. *et al.* The Burden of Primary Liver Cancer and Underlying Etiologies From 1990 to 2015 at the Global, Regional, and National Level: Results From the Global Burden of Disease Study 2015. *JAMA Oncol* **3**, 1683–1691, doi:10.1001/jamaoncol.2017.3055 (2017).
90. Islami, F. *et al.* Proportion and number of cancer cases and deaths attributable to potentially modifiable risk factors in the United States. *CA Cancer J Clin* **68**, 31–54, doi:10.3322/caac.21440 (2018).
91. Brown, J. *et al.* Pretreatment prognostic factors for children with hepatoblastoma— results from the International Society of Paediatric Oncology (SIOP) study SIOPEL 1. *Eur J Cancer* **36**, 1418–1425, doi:10.1016/s0959-8049(00)00074-5 (2000).
92. Pietsch, T. *et al.* Characterization of the continuous cell line HepT1 derived from a human hepatoblastoma. *Lab Invest* **74**, 809–818 (1996).
93. Ellerkamp, V. *et al.* Successful establishment of an orthotopic hepatoblastoma in vivo model in NOD/LtSz-scid IL2Rgamma null mice. *PLoS One* **6**, e23419, doi:10.1371/journal.pone.0023419 (2011).
94. Ong, L. C. *et al.* Effective inhibition of xenografts of hepatocellular carcinoma (HepG2) by rapamycin and bevacizumab in an intrahepatic model. *Mol Imaging Biol* **11**, 334–342, doi:10.1007/s11307-009-0213-4 (2009).
95. Woodfield, S. E. *et al.* A Novel Cell Line Based Orthotopic Xenograft Mouse Model That Recapitulates Human Hepatoblastoma. *Sci Rep* **7**, 17751, doi:10.1038/s41598-017-17665-8 (2017).
96. Fuchs, J., Schmidt, D., Pietsch, T., Miller, K. & von Schweinitz, D. Successful transplantation of human hepatoblastoma into immunodeficient mice. *J Pediatr Surg* **31**, 1241–1246, doi:10.1016/s0022-3468(96)90242-0 (1996).

97. Hata, Y. *et al.* Establishment of an experimental model of human hepatoblastoma. *Cancer* **50**, 97–101, doi:10.1002/1097-0142(19820701)50:1<97::aid-cncr2820500118>3.0.co;2-4 (1982).
98. Desdouets, C., Fabre, M., Gauthier, F., Brechot, C. & Sobczak-Thepot, J. Proliferation and differentiation of a human hepatoblastoma transplanted in the Nude mouse. *J Hepatol* **23**, 569–577, doi:10.1016/0168-8278(95)80064-6 (1995).
99. Nicolle, D. *et al.* Patient-derived mouse xenografts from pediatric liver cancer predict tumor recurrence and advise clinical management. *Hepatology* **64**, 1121–1135, doi:10.1002/hep.28621 (2016).
100. Bissig-Choisat, B. *et al.* Novel patient-derived xenograft and cell line models for therapeutic testing of pediatric liver cancer. *J Hepatol* **65**, 325–333, doi:10.1016/j.jhep.2016.04.009 (2016).
101. Zhu, L. *et al.* Multi-organ Mapping of Cancer Risk. *Cell* **166**, 1132–1146 e1137, doi:10.1016/j.cell.2016.07.045 (2016).
102. Malogolowkin, M. H. *et al.* Complete surgical resection is curative for children with hepatoblastoma with pure fetal histology: a report from the Children's Oncology Group. *J Clin Oncol* **29**, 3301–3306, doi:10.1200/JCO.2010.29.3837 (2011).
103. Kats, D. *et al.* Volasertib preclinical activity in high-risk hepatoblastoma. *Oncotarget* **10**, 6403–6417, doi:10.18632/oncotarget.27237 (2019).
104. Zhang, S. *et al.* The Hippo Effector Transcriptional Coactivator with PDZ-Binding Motif Cooperates with Oncogenic beta-Catenin to Induce Hepatoblastoma Development in Mice and Humans. *Am J Pathol* **190**, 1397–1413, doi:10.1016/j.ajpath.2020.03.011 (2020).
105. Schramek, D. *et al.* Direct in vivo RNAi screen unveils myosin Ila as a tumor suppressor of squamous cell carcinomas. *Science* **343**, 309–313, doi:10.1126/science.1248627 (2014).
106. Vervoort, S. J., van Boxtel, R. & Coffer, P. J. The role of SRY-related HMG box transcription factor 4 (SOX4) in tumorigenesis and metastasis: friend or foe? *Oncogene* **32**, 3397–3409, doi:10.1038/onc.2012.506 (2013).
107. Brognard, J., Zhang, Y. W., Puto, L. A. & Hunter, T. Cancer-associated loss-of-function mutations implicate DAPK3 as a tumor-suppressing kinase. *Cancer Res* **71**, 3152–3161, doi:10.1158/0008-5472.CAN-10-3543 (2011).
108. Cai, Z. *et al.* Oncogenic miR-17/20a Forms a Positive Feed-forward Loop with the p53 Kinase DAPK3 to Promote Tumorigenesis. *J Biol Chem* **290**, 19967–19975, doi:10.1074/jbc.M115.661504 (2015).
109. Takahashi, M. *et al.* The tumor suppressor kinase DAPK3 drives tumor-intrinsic immunity through the STING-IFN-beta pathway. *Nat Immunol* **22**, 485–496, doi:10.1038/s41590-021-00896-3 (2021).
110. Steklov, M. *et al.* Mutations in LZTR1 drive human disease by dysregulating RAS ubiquitination. *Science* **362**, 1177–1182, doi:10.1126/science.aap7607 (2018).
111. Arafeh, R. *et al.* Recurrent inactivating RASA2 mutations in melanoma. *Nat Genet* **47**, 1408–1410, doi:10.1038/ng.3427 (2015).
112. Luo, J. *et al.* DUSP9 Suppresses Proliferation and Migration of Clear Cell Renal Cell Carcinoma via the mTOR Pathway. *Onco Targets Ther* **13**, 1321–1330, doi:10.2147/OTT.S239407 (2020).

113. Liu, Y., Lagowski, J., Sundholm, A., Sundberg, A. & Kulesz-Martin, M. Microtubule disruption and tumor suppression by mitogen-activated protein kinase phosphatase 4. *Cancer Res* **67**, 10711–10719, doi:10.1158/0008-5472.CAN-07-1968 (2007).
114. Rah, B. *et al.* PAWR-mediated suppression of BCL2 promotes switching of 3-azido withaferin A (3-AWA)-induced autophagy to apoptosis in prostate cancer cells. *Autophagy* **11**, 314–331, doi:10.1080/15548627.2015.1017182 (2015).
115. Li, W. C., Ralphs, K. L. & Tosh, D. Isolation and culture of adult mouse hepatocytes. *Methods Mol Biol* **633**, 185–196, doi:10.1007/978-1-59745-019-5_13 (2010).
116. Cheng, C. *et al.* Latent cellular analysis robustly reveals subtle diversity in large-scale single-cell RNA-seq data. *Nucleic Acids Res* **47**, e143, doi:10.1093/nar/gkz826 (2019).
117. Chen, W. *et al.* UMI-count modeling and differential expression analysis for single-cell RNA sequencing. *Genome Biol* **19**, 70, doi:10.1186/s13059-018-1438-9 (2018).

Tables

Tables 1-2 are in the supplemtary files section.

Figures

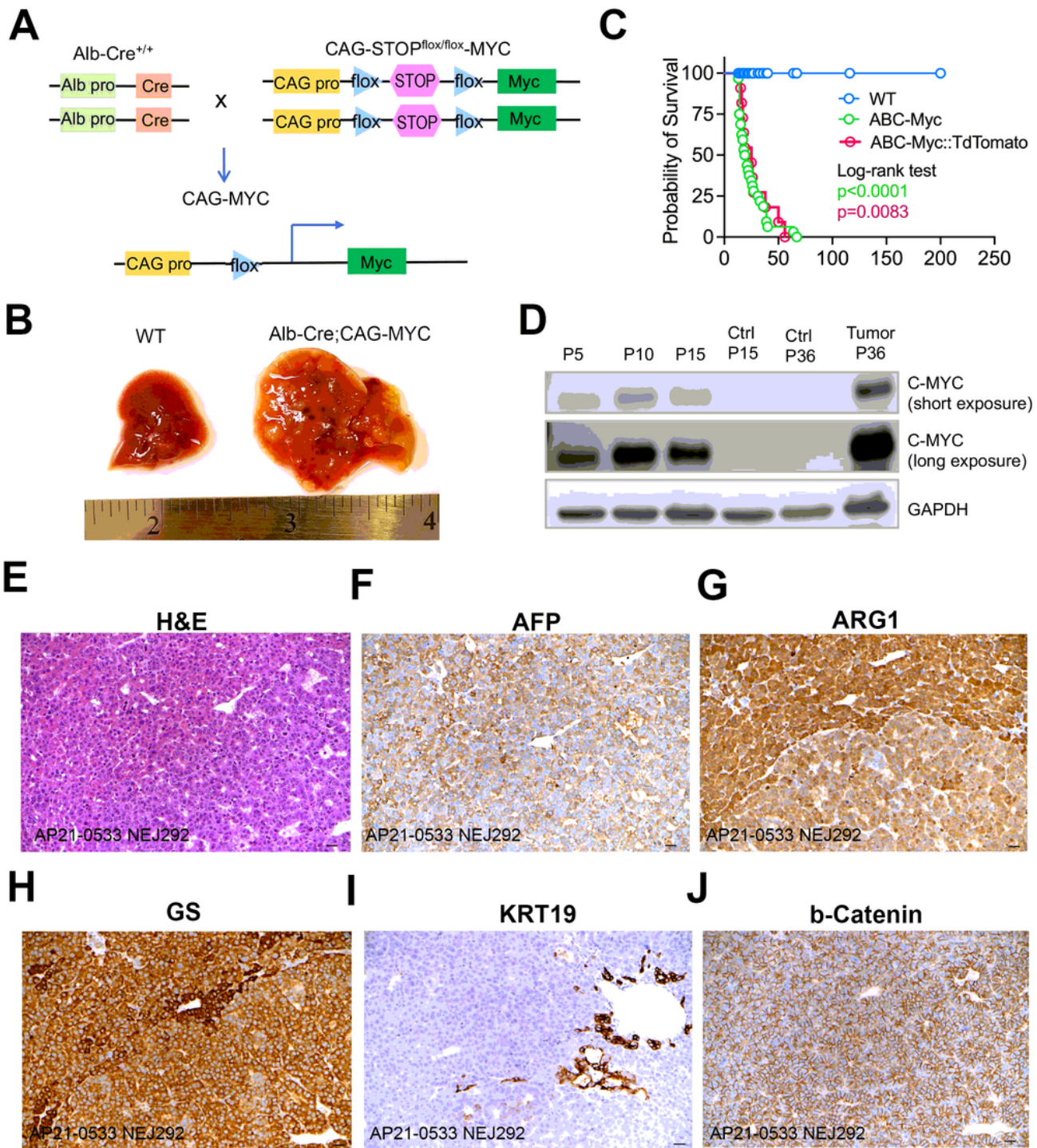


Figure 1.

Figure 1

ABC-Myc drives hepatoblastoma development

(A) Breeding strategy to generate Alb-Cre;CAG-Myc (ABC-Myc).

(B) Hepatomegaly with tumor nodules.

(C) Inferior overall survival of ABC-Myc, and ABC-Myc/TdTomato mice, respectively.

(D) Western blot showing overexpression of C-MYC in livers of ABC-Myc livers at postnatal day 5, 10,15 and 36 in comparison with controls at postnatal day 15 and 36.

(E) Hematoxylin and Eosin (H&E) shows histology of ABC-Myc tumor. Scale bar = 25mM

(F-J) Immunostaining of AFP, arginase (ARG1) glutamine synthetase (GS), cytokeratin 19 (KRT19) and b-catenin. Scale bar = 25mM

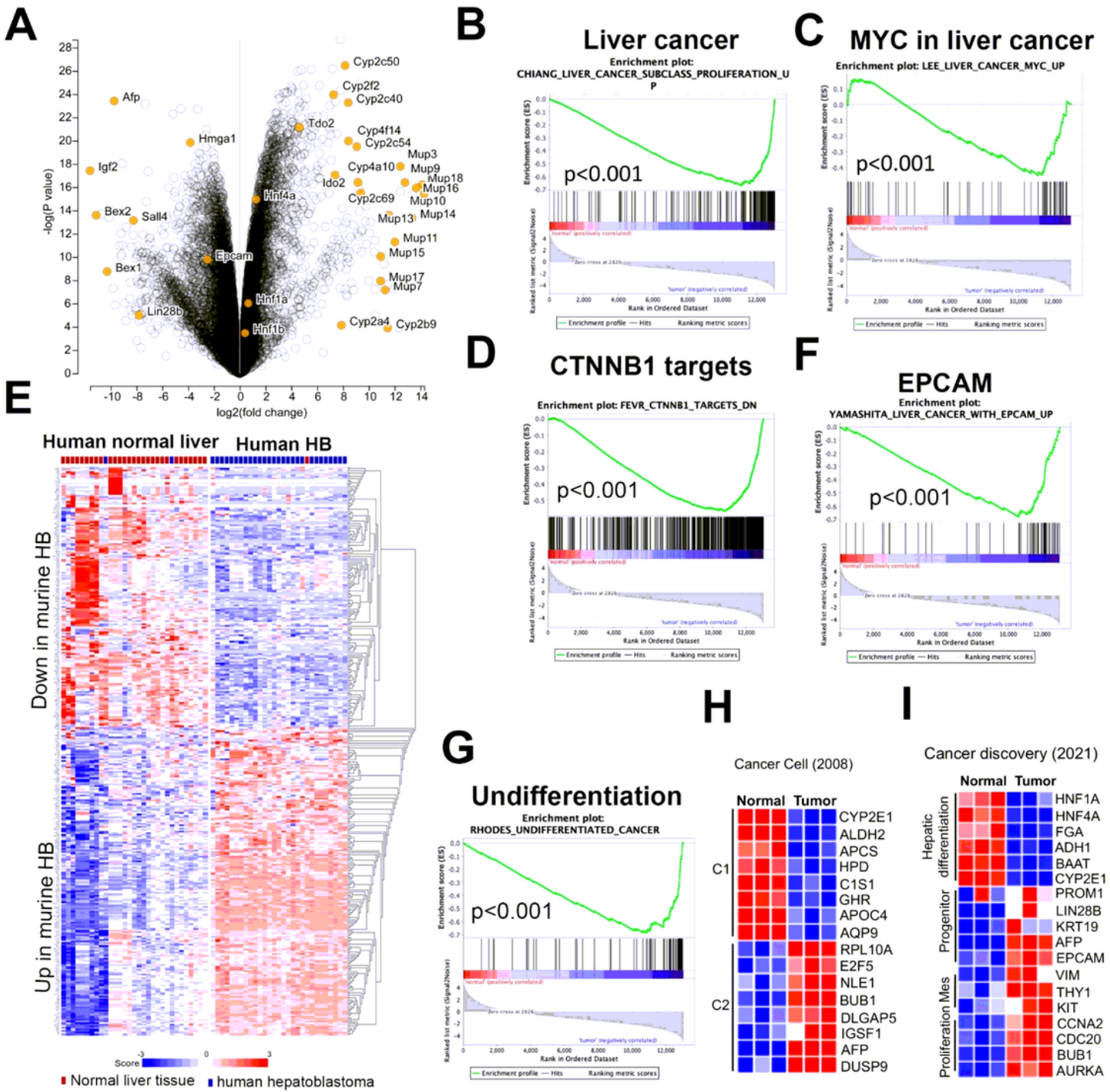


Figure 2

Figure 2

Signaling pathways in ABC-Myc tumor cells resemble those in human hepatoblastoma with poor outcome

(A) Volcano plot showing differentially expressed genes in ABC-Myc tumors vs normal mouse livers. (B-D) GSEA showing gene signatures or signaling pathways highly upregulated in ABC-Myc hepatoblastoma.

(E) Heat map showing the top differentially expressed genes in ABC-Myc tumors vs age-matched normal livers are similarly altered in human HB tumors.

(F, G) GSEA showing stem cell gene signatures highly upregulated in ABC-Myc hepatoblastoma.

(H) Heatmap showing expression of C2 signature of high-risk human hepatoblastoma in ABC-Myc tumor cells.

(I) Heatmap showing high expression of 'progenitor' and 'proliferation' signatures of high-risk human hepatoblastoma in ABC-Myc tumor cells.

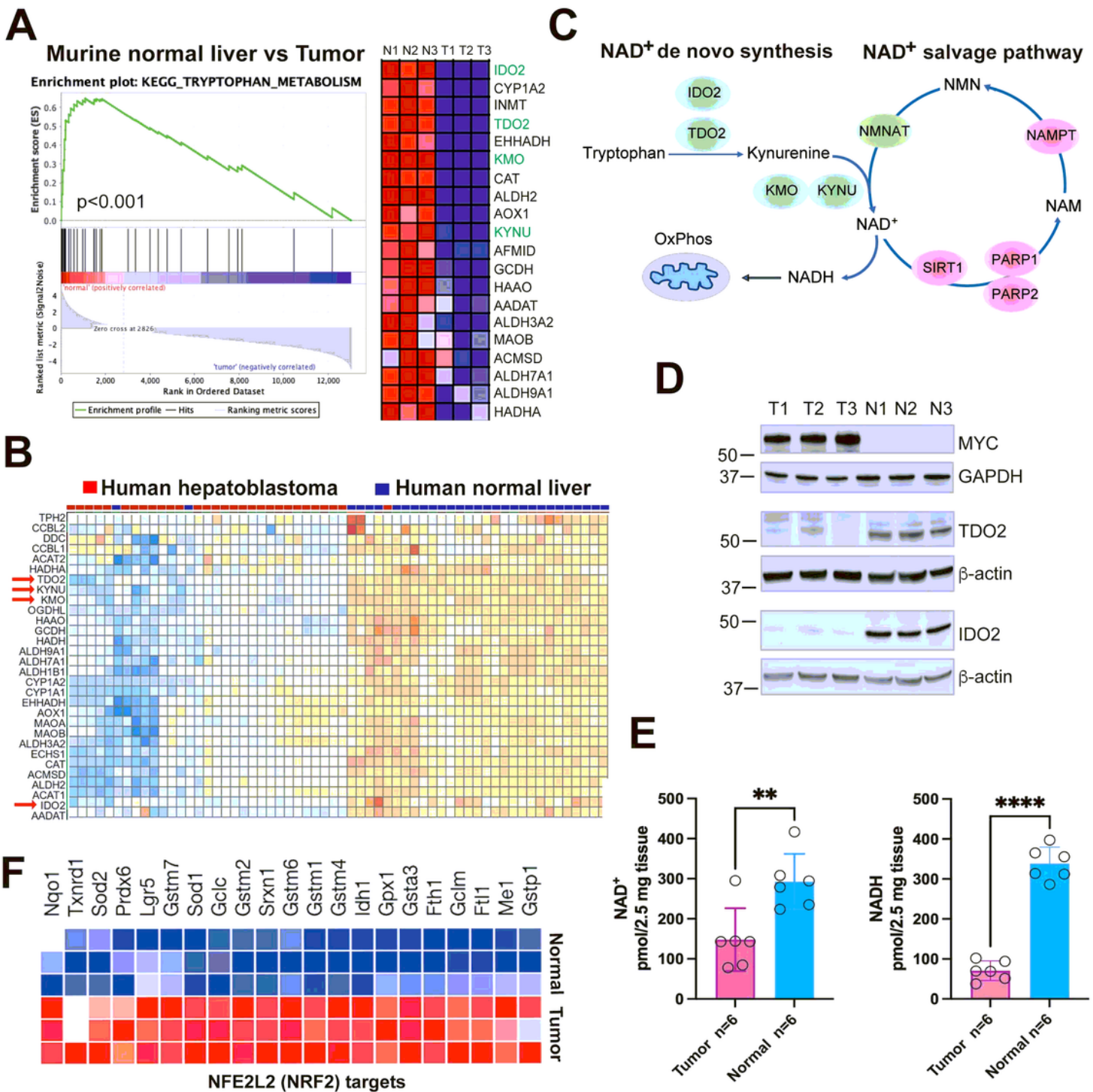


Figure 3

Figure 3

ABC-Myc tumors have common dysregulated metabolic pathways with human hepatoblastoma.

(A) GSEA showing downregulation of tryptophan metabolism pathway (left) and heatmap gene list (right) of ABC-Myc hepatoblastoma.

- (B) Heatmap showing downregulation of tryptophan metabolism pathway in human hepatoblastoma (GSE104766).
- (C) Downregulation of de novo and salvage synthesis of NAD⁺ pathways in ABC-Myc hepatoblastoma. Green =down, Pink =up.
- (D) Western blot showing downregulation of TDO2 and IDO2 in ABC-Myc tumor samples (n=3) vs normal livers (n=3). Unpaired student t test.
- (E) Quantification of NAD⁺ and NADH levels in ABC-Myc tumor samples (n=6) vs normal livers (n=6).
- (F) Heatmap showing upregulation of NFE2L2 target genes in ABC-Myc hepatoblastoma samples vs normal livers.

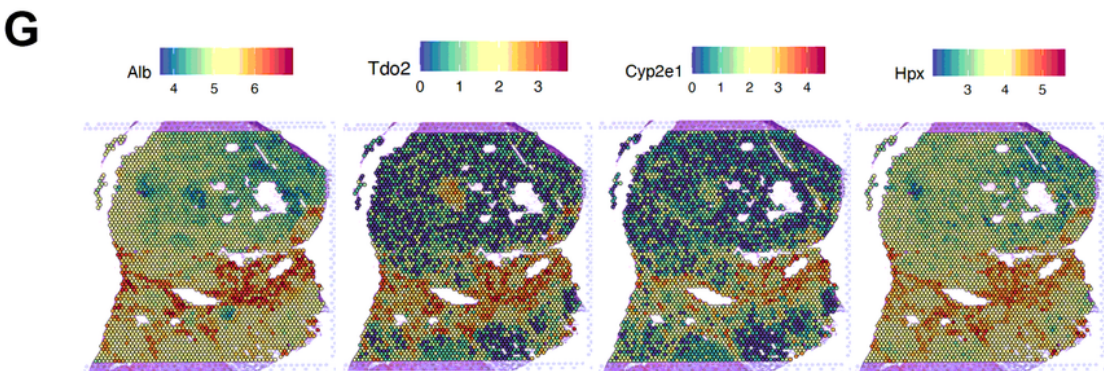
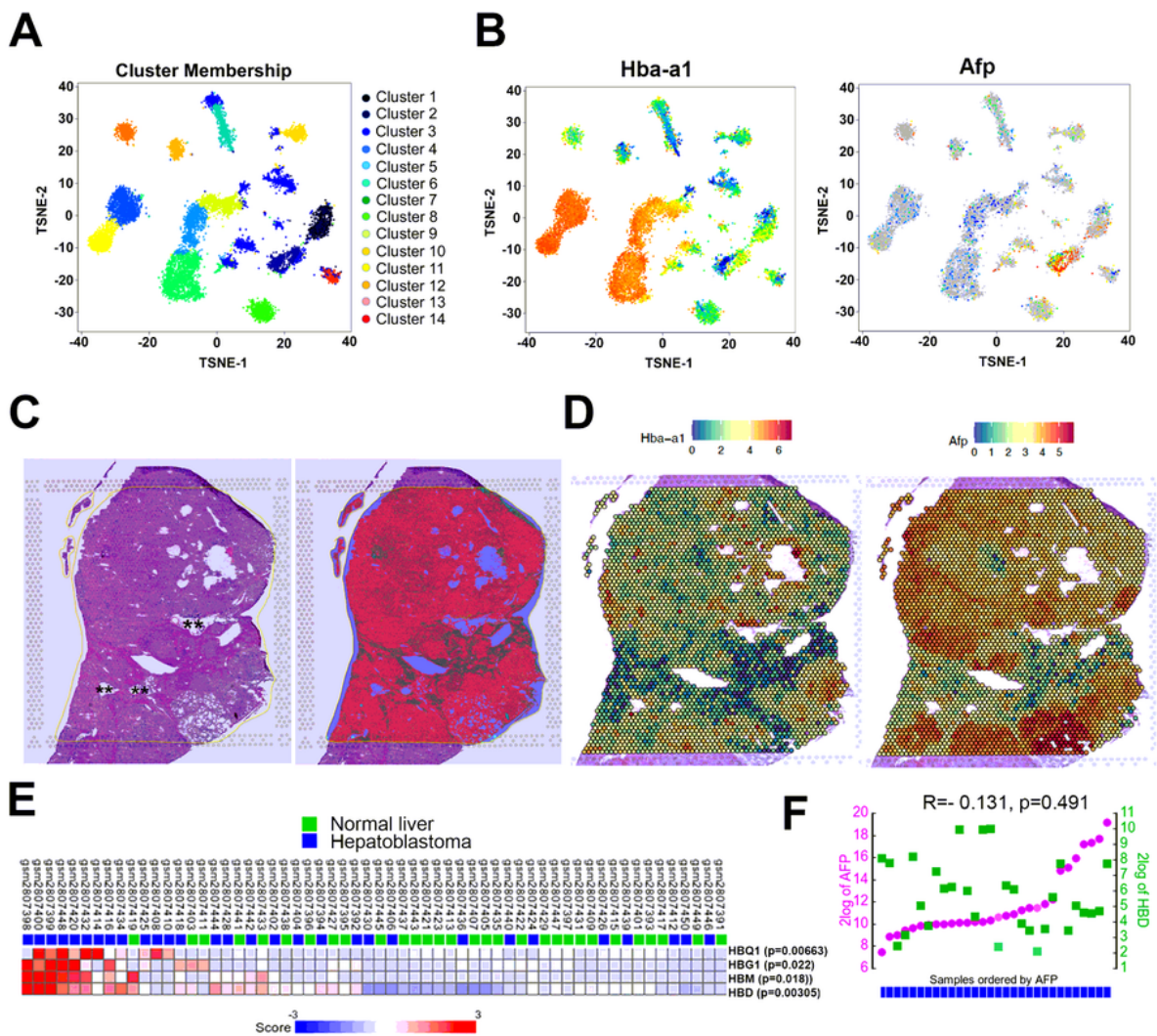


Figure 4

Figure 4

scRNA-seq and spatial transcriptomic analysis of ABC-Myc tumors reveals the heterogeneity of hepatoblastoma cells

(A) Clusters of single cell RNA-sequencing of fresh ABC-Myc hepatoblastoma tumor tissue.

- (B) scRNA-seq identifying hemoglobin high and Afp high clusters.
- (C) ABC-Myc tissue section for spatial transcriptome analysis. (left) Tissue section. ** portal vein. (Right) Annotation of pathological features of tissue section. Red: Regions interpreted to be neoplastic tissue, Green: Regions interpreted to be non-neoplastic appearing tissue, Yellow: Foci interpreted to be extramedullary hematopoiesis, Dark blue: Glass/Clear spaces, Light blue: Tissue folds and/or artifacts in the section.
- (D) Plot for spatial transcriptomic reads of Hba-a1 and Afp.
- (E) The differential expression of hemoglobin genes in human hepatoblastoma vs normal livers (GSE104766). P value calculated by unpaired t test.
- (F) Expression of *AFP* and *HBD* in human hepatoblastoma samples with Spearman correlation.
- (G) Expression of liver-specific genes in spatial transcriptomic analysis.

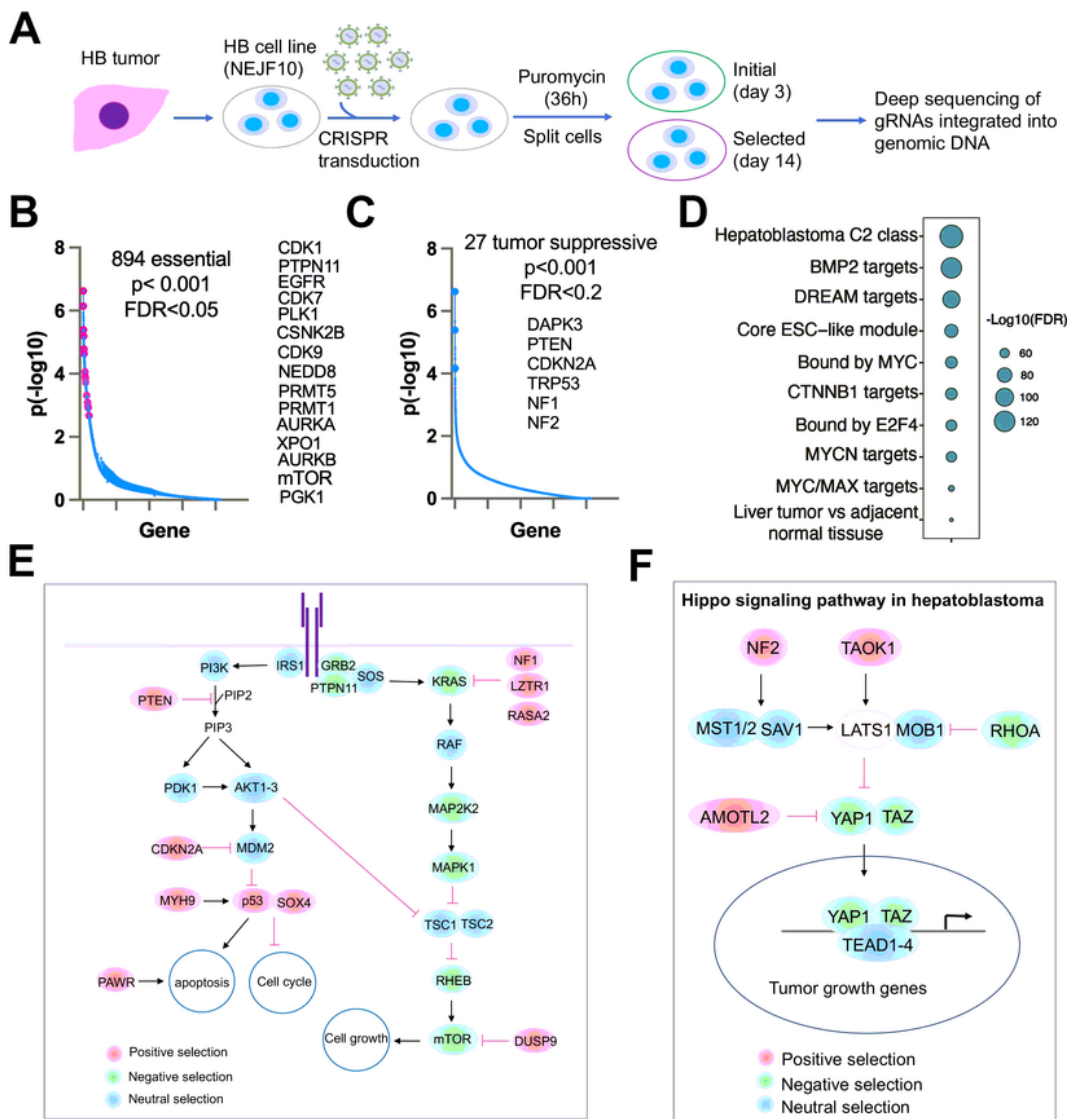


Figure 5

Figure 5

Cancer dependency genes and oncogenic pathways of hepatoblastoma cells.

(A) Genome-wide CRISPR screen of cancer dependency genes.

(B, C) Cancer essential genes and tumor suppressors identified in ABC-Myc cell line.

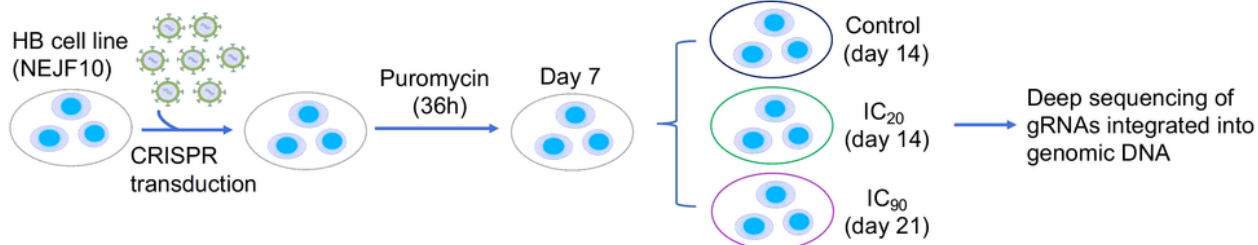
(D) Pathway enrichment in cancer dependency genes identified in ABC-Myc cell line.

(E, F) Canonical cancer pathways enriched in genes identified by CRISPR screen in ABC-Myc cell line.

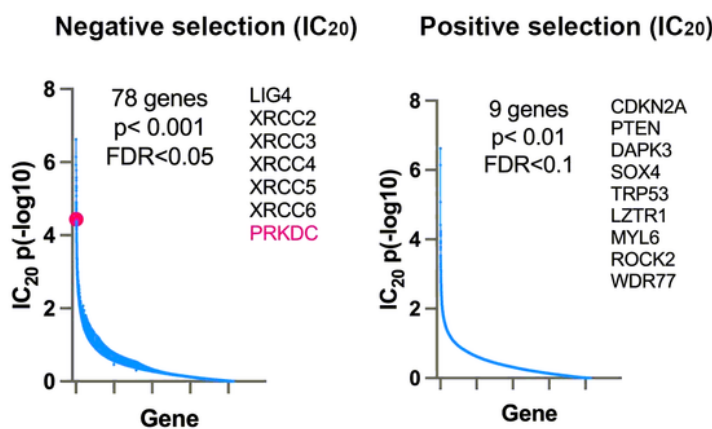
(G) Cancer dependency genes identified in human hepatoblastoma Huh6 cell line.

(H) ABC-Myc and human hepatoblastoma cell lines share conserved cancer dependency genes.

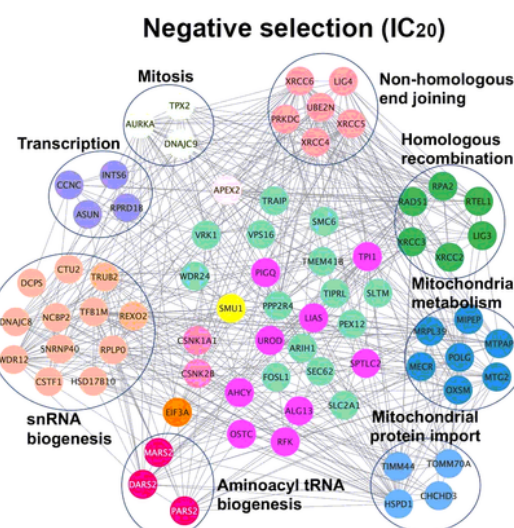
A



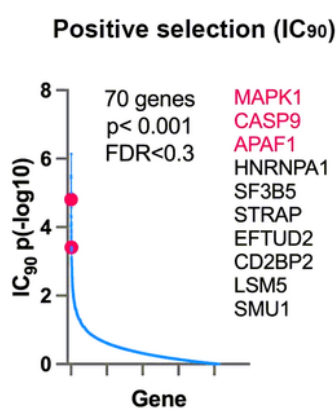
B



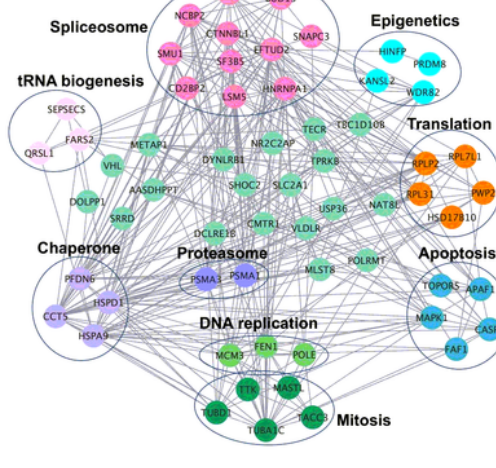
C



D



E



F

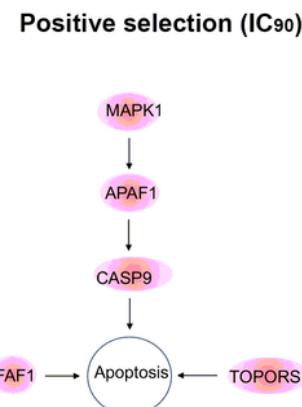


Figure 6

Figure 6

Identification of genetic modifiers of chemotherapy.

- (A) Genome-wide CRISPR screening for the genetic modifiers of doxorubicin in ABC-Myc cell line.
- (B) Negative selection and positive selection under IC₂₀ of doxorubicin.
- (C) Pathways within a protein-protein interaction network enriched in negative selection under IC₂₀ of doxorubicin. Network analysis performed using STRING program (<https://string-db.org/>).
- (D) Positive selection under IC₉₀ of doxorubicin.
- (E, F) Pathways within a protein-protein interaction network enriched in negative selection under IC₉₀ of doxorubicin (E) and apoptotic pathway (F). Network analysis performed using STRING program (<https://string-db.org/>).

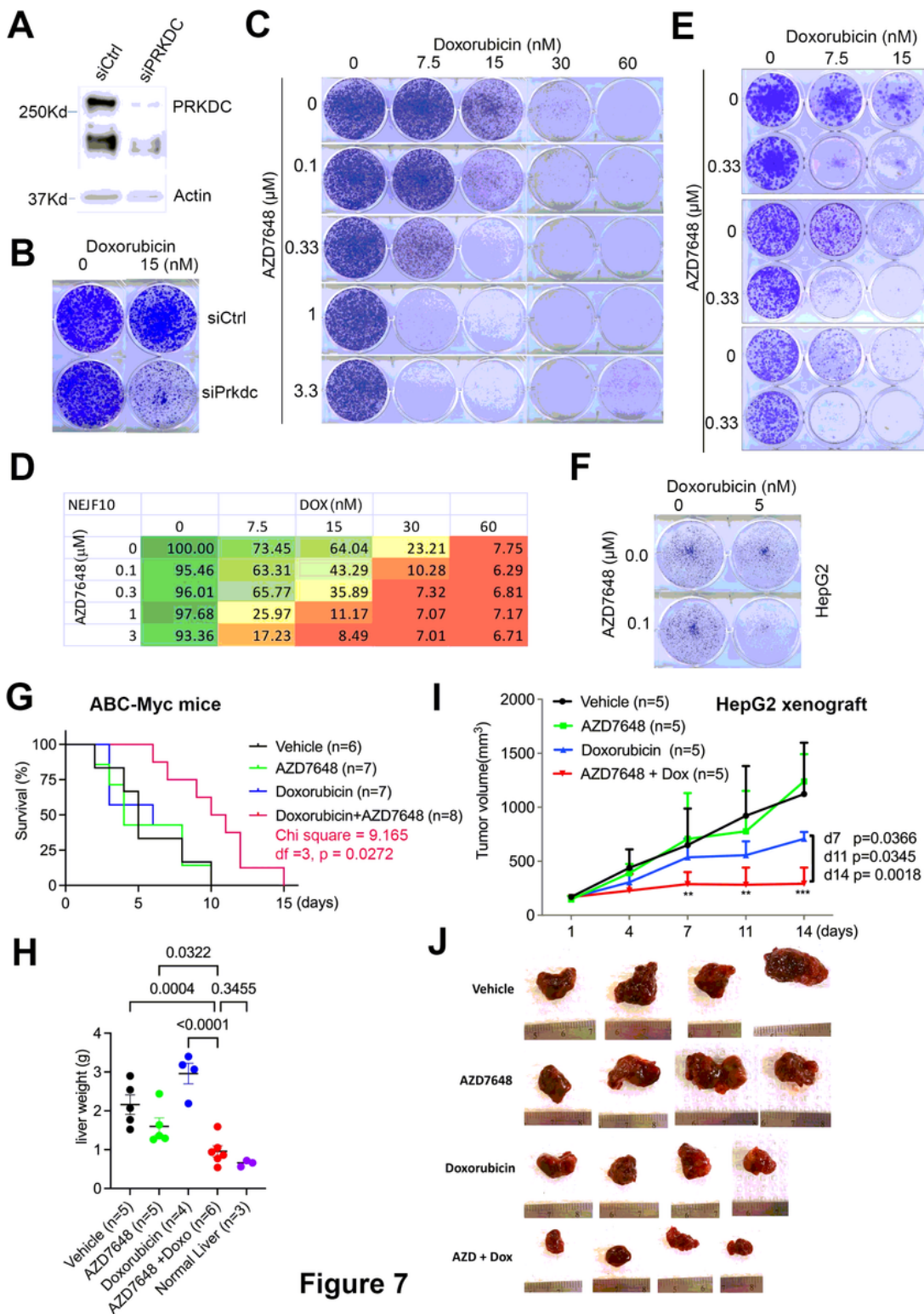


Figure 7

Figure 7

Combination of doxorubicin and PRKDC inhibitor has a better anticancer efficacy.

(A) Western blot showing knockdown of PRKDC in NEJF10 cells.

- (B) Colony formation showing the effect of combination of PRKDC knockdown and doxorubicin treatment for 4 days (bottom).
- (C) Colony formation showing the synergistic effect of combination of different concentrations of doxorubicin and AZD7648 to treat NEJF10 for 5 days.
- (D) Prestoblue assay showing the synergistic effect of combination of different concentrations of doxorubicin and AZD7648 to treat NEJF10 for 4 days. The mean readouts for combination treatment are normalized to control wells treated with “0” concentration of drugs.
- (E) Colony formation for NEJF1, NEJF2, NEJF4 treated with doxorubicin and AZD7648 for 5 days.
- (F) Colony formation for HepG2 treated with doxorubicin and AZD7648 for 8 days.
- (G) Survival rate for ABC-Myc treated with doxorubicin (0.75 mg/kg, twice weekly) and AZD7648 (50mg/kg, twice daily). P value calculated by log-rank (Mantel-Cox) test method.
- (H) Liver weight after treatment in each group of ABC-Myc mice and normal liver in age matching mice. P value calculated by student t test.
- (I) Tumor volume for each treatment group of HepG2 xenografts with doxorubicin (1.0 mg/kg, twice weekly) and AZD7648 (50mg/kg, twice daily). p value calculated by student t test for two groups at each time point.
- (J) Individual tumor size in each group of HepG2 collected at day 18.

Supplementary Files

This is a list of supplementary files associated with this preprint. Click to download.

- [SupplementalInformation.pdf](#)
- [Tables.docx](#)